Preparation, Photophysical and Electrochemical Properties of Eu(III) Complex-Smectite Hybrid Material

February 2025

Rong Cao

Graduate School of Science and Engineering

Chiba University

（千葉大学審査学位論文）

Preparation, Photophysical and Electrochemical Properties of Eu(III) Complex-Smectite Hybrid Material

Eu(III)錯体−スメクタイト複合材料の調製と光物理および電気化学特性

February 2025

Rong Cao

Graduate School of Science and Engineering

Chiba University

Preface

Eu(III) complexes with organic ligands have garnered significant interest due to their unique photophysical properties, such as narrow emission bands, long decay times, and large Stokes shifts, making them applicable in display devices, chemical sensors, and bioimaging. However, the practical application of pure Eu(III) complexes has some limitations because of their poor thermal and photochemical stabilities. Therefore, in-depth studies on luminescent hybrid materials incorporating Eu(III) complexes within a matrix have been extensively conducted to enhance emission intensity and stability. Additionally, electrochemically controlled emission and coloration display technologies based on Eu(III) complexes have sparked significant scientific interest. The controllable electroluminescent properties of these materials are crucial for functional devices like display devices. However, to realize structurally simple multimode display devices, designing novel materials that respond to external stimuli to regulate both emission and reflection is critical. Compared to traditional matrix, smectite have attracted significant interest in various applications due to its unique properties, including excellent chemical stability, and cation exchange/intercalation capabilities. Therefore, this thesis focuses on investigation of photophysical and electrochemical properties of Eu(III) complexes hybridized with smectite.

The photoluminescence properties of Eu(III) complex was investigated in Chapter 2. In this research, an efficient luminescent hybrid materials were prepared by hybridizing the Eu(III) complex with smectite. In this hybrid solution system, the Eu(III) complex exhibited high emission intensity (>1.4 times) and improved quantum efficiency interacted with smectite. Moreover, we prepared a highly luminescent and transparent polymeric film by incorporating $Eu(tta)_3phen$/smectite hybrid material into a polymer (PMMA) matrix. With the addition of the smectite, the emission intensity and surface smoothness of the polymeric film were improved. This strategy presents a novel opportunity for high-luminescence imaging devices.

After examining the photophysical properties of the Eu(III) complex-smectite hybrid material, its electrofluorochromic (EFC) of electrochemical properties were investigated, characterized by changes in emission properties by electrochemical redox reaction. In Chapter 3, a novel display device was constructed by immobilizing a Eu(III) complex and an electrochromic viologen derivative (HV^{2+}) onto a smectite-modified electrode. Under an open circuit condition, the Eu(III) complex exhibited red emission. The electrochemically colored $HV^{\bullet+}$ species (cyan color) quenched the red emission of the Eu(III) complex by applying voltage. This emission intensity change was achieved

via both energy transfer from the excited state of Eu(III) complex to the reduced state of $HV^{\bullet+}$ and reabsorption of the luminescence by the colored $HV^{\bullet+}$ species. This modulation of electrically controlled emission and coloration in clay matrix offers the possibility for the advanced electrochemical display devices.

CAO RONG

Acknowledgement

As I write this, my journey as a student is coming to an end. Time flies—it has already been three years since I began my studies at Chiba University. Over these years, I have been fortunate to receive support from professors, classmates, friends, and many others whose names I may not know. The kindness and wisdom of my professors will always stay with me. I would like to extend my heartfelt gratitude to my advisors, Professor Norihisa Kobayashi and Professor Kazuki Nakamura, for their invaluable guidance, support, and encouragement. From selecting research topics to conducting experiments and writing my dissertation, their mentorship made it possible for me to complete my doctoral studies. Their warmth and kindness made my experience as an international student feel welcoming and enriched. The professors' optimism, calm demeanor, rigorous scholarship, and humility will always serve as guiding principles in my life. I wish them the very best and hope that the years ahead bring them all the wonderful things they truly deserve.

I would also like to express my heartfelt gratitude to my fellow lab members, who helped me quickly adapt to lab life and guided me in using various experimental instruments. I am also deeply appreciative of the PhD students. Collaborating with each of you has been a pleasure, and it has truly enriched my research experience.

I would like to express my sincere appreciation for the financial support provided by the JST Foundation.

I am also incredibly grateful to my friends. When I first arrived in Japan, I faced feelings of worry, helplessness, loneliness, and moments of doubt. Then I met them, they brought smiles, joy, warmth, and beauty into my studies and life. For that, I am profoundly thankful.

Last, but not the least, my deepest gratitude goes to my family and my boyfriend for their unwavering care and support throughout my academic journey. Regardless of the challenges or requests I faced, they were always there, providing comfort and encouragement. They helped me stay optimistic, believe in the good, and hold on to hope and aspirations for the future.

"May your life set sail, heading towards great ideals." I dedicate this dissertation to all those who have supported me along the way, and to the passionate version of myself that guided me through this journey.

CAO RONG

Content

Chapter 1

General Introduction

Chapter 1 General Introduction

1.1 Lanthanide complex

1.1.1 Concept of lanthanide complex

The lanthanide elements (Ln) comprise a group of 15 elements, including lanthanum (La), cerium (Ce), praseodymium (Pr), neodymium (Nd), promethium (Pm), samarium (Sm), europium (Eu), gadolinium (Gd), terbium (Tb), dysprosium (Dy), holmium (Ho), erbium (Er), thulium (Tm), ytterbium (Yb), and lutetium (Lu)， as illustrated in **Figure 1-1**. Lanthanide complexes possess unique luminescent properties that are closely related to the transitions of lanthanide ions between different energy levels[1]. The influence of the crystal field on these ions is limited due to the shielding effect of the outer-shell electrons. However, because of the relatively large electron spin-orbit coupling constant, the energy levels can split, leading to a rich array of electronic energy levels. These energy levels can emit nearly 30,000 observable spectral lines through f-f configuration transitions or f-d configuration transitions, with their fluorescence emission covering the ultraviolet, visible, and infrared regions[2, 3]. The characteristic emission spectra of these ions are primarily determined by the intrinsic properties of the rare earth ions themselves. For example, Eu^{3+} emits red fluorescence, Tb^{3+} produces green fluorescence, and Sm^{3+} emits orange fluorescence. The luminescence of most Ln^{3+} ions arises from electron transitions within the internal 4f orbitals. The fully occupied 5s and 5p subshells provide effective shielding for these 4f orbitals, rendering f-f transitions less susceptible to external magnetic fields and crystal fields[4]. Consequently, most Ln^{3+} ions exhibit narrow-band, sharp-line emissions. This high color purity, combined with the relative immunity to environmental factors, makes the luminescence of Ln^{3+} ions highly recognizable. For instance, Eu^{3+} typically emits characteristic red fluorescence in the 610-620 nm range, making it an ideal candidate for luminescent probe materials due to its distinct f-f transition features[5-7].

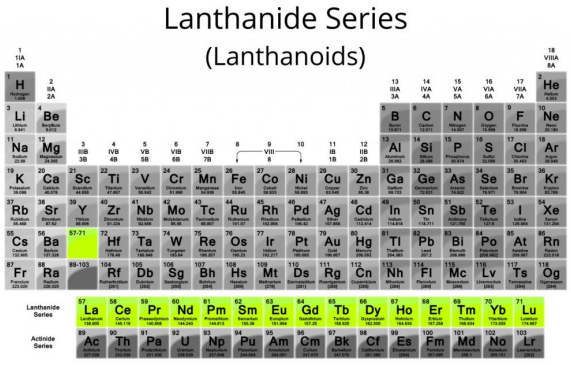

Figure 1-1 Rare earth elements in periodic table.

1.1.2 Luminescence of Lanthanide complex

Due to the symmetry-forbidden nature of f-f electronic transitions, Ln^{3+} ions exhibit inherently low molar absorption coefficients in the ultraviolet and visible regions, leading to weak luminescence intensity. To enhance the luminescence efficiency, a widely adopted approach involves forming coordination complexes with appropriate organic ligands. When these ions coordinate with organic compounds such as crown ethers, carboxylic acids, or β-diketones, the corresponding fluorescence intensity is significantly enhanced[8-13]. This phenomenon was first discovered by Weissman in the early 1940s[14]. The luminescence mechanism relies on energy transfer from the ligands to the central ion, allowing the rare-earth ion to emit its characteristic intense luminescence. Due to their relatively large ionic radii, rare-earth ions generally exhibit high coordination numbers, most commonly 8 or 9.

Organic ligands with conjugated structures possess strong light absorption capabilities. By transferring the absorbed energy to the central rare-earth ion, they effectively enhance its luminescence intensity, a phenomenon referred to as the "antenna effect"[15-19]. As shown in **Figure 1-2**, the antenna effect can be illustrated in the following figure, where the photophysical process of fluorescence generation is typically described in three steps. **1:** The organic ligand molecules are excited by ultraviolet radiation, transitioning from the ground state (S_0) to a vibrational energy level of the first singlet excited state (S_1). Subsequently, the molecules undergo internal conversion, relaxing to the lowest vibrational level of the S_1 state. At this stage, the singlet excited molecules can either return directly to the ground state through radiative decay, emitting fluorescence from the ligands, or undergo non-radiative intersystem crossing to the triplet excited state (T_1). **2:** The triplet excited state may deactivate radiatively to the ground state, emitting ligand phosphorescence, or transfer its energy non-radiatively to an excited energy level of the rare-earth ion ($^5D_0$). **3:** The rare earth

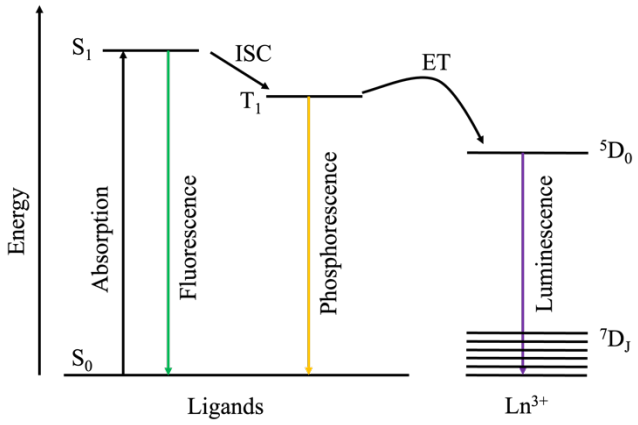

Figure 1-2 Schematic depiction of the antenna effect of lanthanide complex.

ion in its excited state then relaxs through radiative or non-radiative transition to a lower energy level, emitting the characteristic sharp-line luminescence of the rare earth ion.

The coordination saturation number of rare-earth ions generally falls within the range of 8 to 10. If the rare earth ion coordinates only with anionic ligands (the first ligand), the coordination number requirement may not be fully satisfied. In such case, the introduction of a secondary ligand becomes necessary[20-24]. In the rare-earth europium complex system, introducing a secondary ligand can partially or entirely replace coordinated water molecules, thereby minimizing energy loss associated with high-frequency O-H vibrations and enhancing the fluorescence efficiency of the complex. If the secondary ligand possesses a highly conjugated structure and its lowest triplet excited state is well aligned with the excited-state energy level of the rare-earth ion, the absorbed energy can be effectively transferred either directly to the central ion or via the primary ligand, significantly boosting the luminescence efficiency of the complex[25, 26].

Photoluminescence properties of Eu(III) complex

Trivalent europium ions (Eu^{3+}) within lanthanide ions are renowned for their characteristic red luminescence. Compared to other lanthanide ions, Eu^{3+} is particularly advantageous due to its even number of 4f electrons and non-degenerate ground state, characterized by a total angular momentum quantum number $J = 0$. Consequently, Eu(III) complexes exhibit relatively simple and well-defined emission spectra, facilitating spectral analysis[5]. As shown in **Figure 1-3**, most Eu(III) complexes display intense emission spectra. These emission peaks correspond to the transitions from the excited state ($^5D_0$) to the ground state (^7F_J), specifically the $^5D_0 \rightarrow {}^7F_J$ transitions. Although the 4f orbitals of Eu^{3+} are effectively shielded, their electronic structure is still subject to perturbation by the surrounding crystal field. For each J level, the degeneracy is $2J + 1$, the splitting of which depends on the symmetry and ligand field characteristics of the Eu(III) complexes[27].

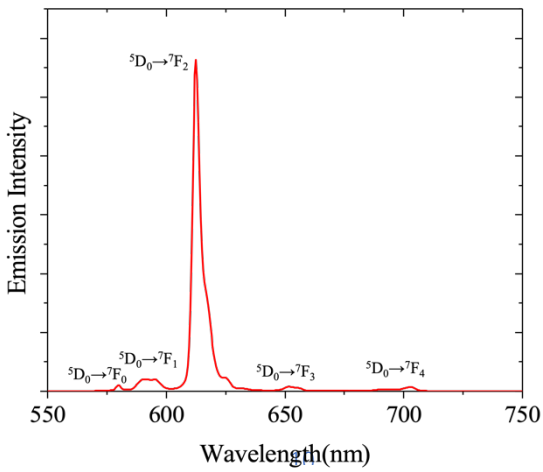

Figure 1-3 Representative emission spectra of Eu(III) complex.

The majority of emission peaks observed in Eu(III) complexes arise from electric dipole (ED) transitions, which are induced by interactions between the Eu^{3+} ion and the electric dipole vector through electric dipole coupling. According to the Laporte selection rule, these intra-configurational ED transitions (f-f transitions) are theoretically forbidden[28]. However, ED transitions are observed in Eu(III) complexes due to the influence of the surrounding environment, which partially allow ED transitions through crystal field effects, *J*-mixing, or vibronic coupling.

The intensities of these ED transitions can be quantitatively analyzed using Judd-Ofelt (JO) theory, which provides a theoretical framework for interpreting the luminescence behavior of Eu(III) complexes. A thorough understanding of these transitions is essential for analyzing and interpreting the luminescence spectra of Eu(III) complexes. Table 1-1 summarizes the key characteristics of the $^5D_0 \rightarrow {}^7F_J$ transitions in the emission spectra, providing an overview of various ED transitions and their contributions to the luminescenct properties of Eu(III) complexes[29].

Table 1-1. Transitions in emission spectra of Eu(III) complex

Transition	Dipole character	Wavelength range(nm)	Remarks
$^5D_0 \rightarrow {}^7F_0$	ED	570-585	Only observed in specific symmetry
$^5D_0 \rightarrow {}^7F_1$	MD	585-600	Intensity largely independent of environment
$^5D_0 \rightarrow {}^7F_2$	ED	610-630	Hypersensitive transition; intensity very strongly dependent on environment
$^5D_0 \rightarrow {}^7F_3$	ED	640-660	Forbidden transition
$^5D_0 \rightarrow {}^7F_4$	ED	680-710	Intensity dependent on ligand environment, but no hypersensitivity

Notably, the observable $^5D_0 \rightarrow {}^7F_0$ transition shows that the Eu^{3+} is situated in a specific symmetry[30], despite this transition being strictly forbidden under standard Judd-Ofelt theory. The $^5D_0 \rightarrow {}^7F_1$ transition is the only MD transition in the table, inherently allowed by the Laporte selection rule. However, its intensity remains relatively weak and comparable to that of the induced ED transitions[31]. Unlike ED transitions, the radiative rate of the MD transition is independent of changes in the local environment surrounding the Eu^{3+}.

The $^5D_0 \rightarrow {}^7F_2$ and $^5D_0 \rightarrow {}^7F_4$ transitions exhibit hypersensitivity and normal sensitivity to the surrounding environment of the Eu^{3+} ions [32]. In Eu(III) complexes containing β-diketonate ligands, the $^5D_0 \rightarrow {}^7F_2$ transition exhibits a more intense

hypersensitive emission peak than other transitions. The intensity of the $^5D_0 \rightarrow {}^7F_2$ transition is directly proportional to the value of the Judd-Ofelt intensity parameter Ω_2[33, 34]. Additionally, the $^5D_0 \rightarrow {}^7F_2$ transition serves as a valuable indicator of the local site symmetry around the Eu^{3+}. Generally, the integrated intensity ratio (I_{rel}) of the $^5D_0 \rightarrow {}^7F_1$ to $^5D_0 \rightarrow {}^7F_2$ transitions is used to assess the degree of asymmetry surrounding the Eu^{3+} ion, where a higher ratio indicates a lower positional symmetry[35]. The $^5D_0 \rightarrow {}^7F_3$ transition is typically weak due to its forbidden nature under the Judd-Ofelt theory, gaining intensity only through *J* mixing effects[36]. A strong $^5D_0 \rightarrow {}^7F_3$ transition is usually a sign of strong *J* mixing and strong crystal field perturbations. The emission spectra provide valuable information that aids in the study of the optical behavior of Eu(III) complexes and the chemical environment surrounding the Eu^{3+}.

In addition, the energy transfer process provides important insights into the optical properties of the Eu(III) complex. This phenomenon can be analyzed through a set of fundamental photophysical parameters, including emission lifetime (τ), intrinsic quantum yield (Φ_{Ln}), radiative rate constant (k_r), and non-radiative rate constant (k_{nr}), which are derived from the Judd-Ofelt theory[37-39]. Emission lifetime represents the average time of the Eu^{3+} ion spends in the ^5D excited state before transitioning to the ^7F ground state through photon emission (luminescence). Subsequently, the Judd-Ofelt parameters Ω_λ (λ= 2, 4, and 6), along with the k_r and k_{nr}, can be calculated using the equations below[40, 41]:

$$\Omega_\lambda = (2\lambda + 1) \sum_{t=\lambda-1}^{\lambda+1(odd)} \sum_{p=-t}^{t(all)} \frac{|B_{\lambda tp}|^2}{(2t+1)}$$

$$K_r = \frac{64\pi^4 v^3}{3h(2J+1)} \times [\frac{n(n^2+2)^2}{9} \times S_{ed} + n^3 S_{md}$$

$$\tau = \frac{1}{K_r + K_{nr}}$$

$$K_{nr} = \frac{1}{\tau} - K_r$$

Herein, $B_{\lambda tp}$ represents the matrix element quantifying the interaction strength between the rare-earth ion and its surrounding environment for a specific transition. *h* denotes Planck's constant, while *2J+1* corresponds to the degeneracy of the initial state. Additionally, *n* refers to the refractive index. S_{ed} and S_{md} describe the forced electric dipole and magnetic dipole mechanisms, respectively[42, 43].

The Φ_{Ln} represents the quantum yield resulting from the direct excitation of Eu^{3+} and is determined using the following equation:

$$\Phi_{Ln} = \frac{k_r}{k_r + k_{nr}}$$

Based on the aforementioned photophysical parameters, the luminescence efficiency of Eu(III) complexes can be quantitatively assessed, along with the influence of the local environment on their spectral properties and the role of selection rules in governing transition processes across various complexes. These analyses provide crucial theoretical support for understanding the application of rare-earth elements in optical materials, lasers, and light-emitting devices. Furthermore, they provide a solid foundation for the design and development of functional materials with tailored luminescent properties.

1.1.3 Lanthanide hybrid materials of Eu(III) complex

It is well established that rare earth complexes exhibit poor stability and low mechanical strength, which significantly limit their range of potential applications. A commonly employed strategy to address these limitations involves embedding rare-earth complexes into stable and rigid matrices. Embedding rare earth complexes into these matrices not only enhances their photostability and thermal stability but also mitigates the concentration quenching effect. Pioneering studies by researchers such as Bünzli[44, 45], Binnemans[46-48], Carlos[49], Sanchez[50], and Okamoto[51] have successfully demonstrated the incorporation of rare-earth complexes into a diverse range of matrices. These matrices encompass sol-gel materials, mesoporous silica, titania, ionic liquids, polymers, hybrid systems (e.g., silica-polymer hybrids), liquid crystals, zeolites, and functional hosts such as magnetic silica nanospheres.

Sol-gel hybrid material:

The sol gel method is extensively utilized for fabricating high-performance luminescent materials composed of rare-earth complex-inorganic or inorganic/organic hybrid matrices, owing to its simplicity and ease of operation. Silicate-based sol-gel materials are synthesized from $Si(OR)_4$, where R denotes different organic groups. The preparation of sol-gel hybrid materials incorporating lanthanide organic complexes typically involves impregnation, doping, or chemical fixation[52, 53].

Machida[54] employed the sol-gel method to incorporate synthesized Eu^{3+} (Tb^{3+}) bipy complexes into a SiO_2 gel matrix, resulting in composite materials with enhanced luminescence intensity compared to pure rare-earth complexes and improved luminescence stability in humid environments. In addition to single-matrix doping,

rare-earth complexes have also been incorporated into SiO_2-M_xO_y (M = Zr, Ta, B, etc.) mixed oxide matrices, resulting in luminescent materials with high doping levels and superior luminescent properties[55, 56]. Qian at el developed an in-situ synthesis method in which rare-earth ions and organic ligands are simultaneously introduced into the sol-gel precursor solution[57-59]. During the hydrolysis and polycondensation processes, the organic ligands and rare-earth ions are encapsulated within the micro-pores of the gel matrix, and through thermal treatment, rare-earth organic complexes are synthesized in-situ within the gel matrix. Furthermore, as illustrated in the **Figure 1-4**, immobilizing lanthanide complexes onto a silica matrix, collisions between the Eu complexes and water molecules are prevented, thereby reducing energy loss and enhancing the quantum efficiency and intensity of luminescence[60-63].

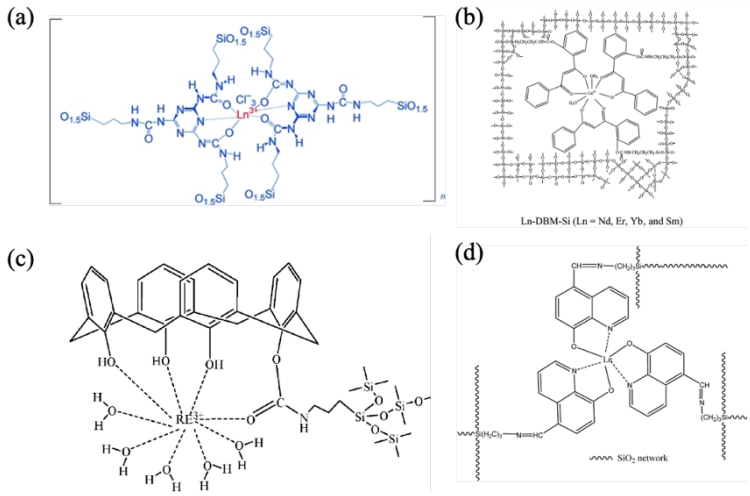

Figure 1-4 Several structures of lanthanide complexes immobilized on silica substrates using chemical immobilization.

Mesoporous hybrid material

In addition to incorporating rare earth complexes into the microporous SiO_2 gel matrix to prepare luminescent hybrid materials, recent literature has increasingly focused on assembling rare earth complexes within the pores of artificially synthesized microporous and mesoporous molecular sieve inorganic crystals, such as MCM-41, MCM-48, SBA-15, and mesoporous organosilica materials (PMOs)[64-72]. The inorganic porous matrix framework exhibit significant rigidity and structural stability, generally remaining chemically inert toward rare earth organic complexes under standard conditions. The multidimensional pore channels or cavities of these matrices effectively isolate guest complexes, while supramolecular interactions between rare

earth complexes and the pore walls of the matrix significantly influence their luminescent properties and stability.

Lanthanide complexes are often introduced into mesoporous materials via simple doping methods[73, 74]. However, challenges such as uneven distribution, aggregation of lanthanide complexes, and their tendency to detach from the matrix. As shown in **Figure 1-5**, researchers have found that covalently bonding the complexes to the mesoporous matrix can address these issues[75-77]. Guo et.al synthesized a novel luminescent mesoporous silica, SBA-15, covalently bonded with ternary lanthanide complex $Eu(TTA)_3phen$ using a co-condensation method followed by a ligand exchange reaction[78]. The resulting $Eu(TTA)_3phen$−SBA-15 exhibits enhanced luminescence intensity, higher quantum efficiency, and excellent thermal stability. Therefore, investigating the fabrication techniques of luminescent hybrid materials that integrate inorganic porous matrix hosts with rare-earth complex guests, along with the intricate host-guest interactions, holds substantial theoretical and practical significance.

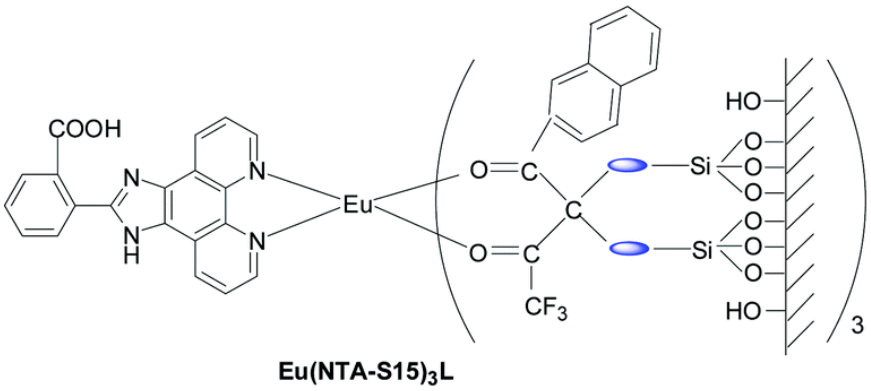

Figure 1-5 The anticipated structure of the mesoporous hybrid material ($Eu(NTA-S15)_3L$).[77]

DNA hybrid material

Deoxyribonucleic acid (DNA) is is a fundamental biomolecule that carries genetic information essential for biological development and life processes. DNA molecules are polymers composed of repeating nucleotides, with each nucleotide consisting of a phosphate group, a sugar (deoxyribose), and a nitrogenous base (**Figure 1-6**). The four nitrogenous bases—adenine (A), thymine (T), cytosine (C), and guanine (G)—form specific hydrogen bonds, giving rise to DNA's characteristic double-helix structure. The two complementary strands of DNA are oriented in opposite directions, exhibiting an antiparallel arrangement.

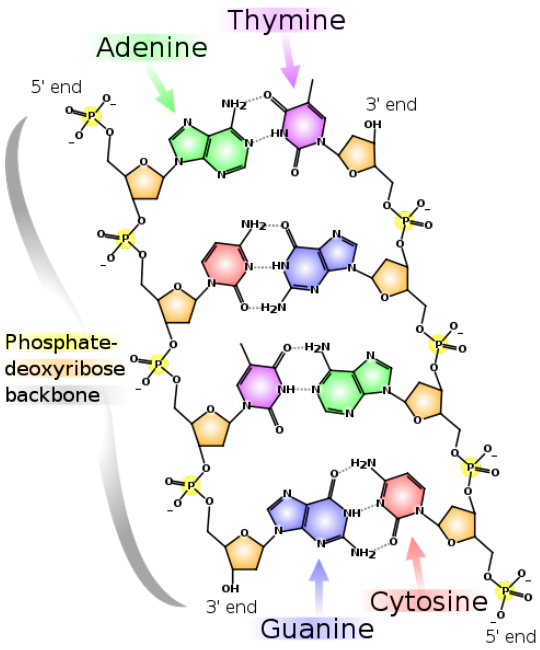

Figure 1-6 Structure of DNA molecule.

Due to its unique structure, DNA can interact with other substances through various mechanisms. The primary modes of DNA interactions include electrostatic interactions, intercalation, and groove binding. These modes interact with DNA in different ways, as illustrated in the schematic diagram in **Figure 1-7**.

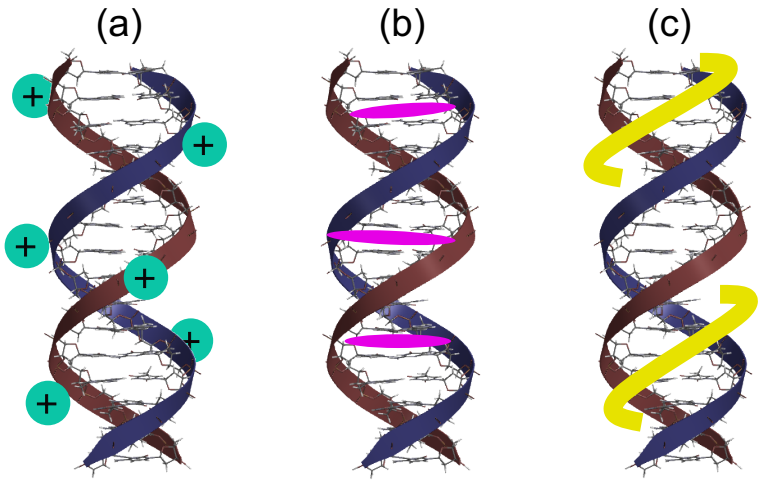

Figure 1-7 Diagrammatic representations of (a) electrostatic interaction, (b) intercalation and (c) groove binding.

However, DNA has poor mechanical properties and may contain mobile ions, which somewhat limits its practical applications. To address these issues, cationic surfactants,

such as CTMA (cetyltrimethylammonium chloride), can be employed for the chemical modification of DNA. CTMA is one of the most commonly used surfactants for enhancing biomolecular characteristics. Compared to unmodified DNA, CTMA-modified DNA (referred to as DNA-CTMA) exhibits significantly increased solubility in organic solvents and enhanced thermal stability, thereby broadening its range of applications.

In recent years, our research laboratory has investigated the impact of DNA and DNA-CTMA on the luminescent properties of Eu(III) complexes. We prepared a hybrid system of DNA/Eu(III) complexes and studied it in aqueous solution. The presence of DNA conferred structural chirality to the Eu(III) complexes and improved their photoluminescent properties compared to the Eu(III) complexes alone. Additionally, the chiral environment introduced by DNA effectively induced circularly polarized luminescence (CPL) signals from the helical Eu(III) complexes[79]. As illustrated in **Figure 1-8**, our research also focused on embedding luminescent Eu(III) complexes into a DNA-CTMA matrix, where the complexes were intercalated within the DNA-CTMA structure [80]. Upon integration into the DNA-CTMA film, the emission performance of the Eu(III) complexes improved. Moreover, when excited through the ligand moiety, the Eu(III) complexes within the DNA-CTMA film exhibited circularly polarized luminescence.

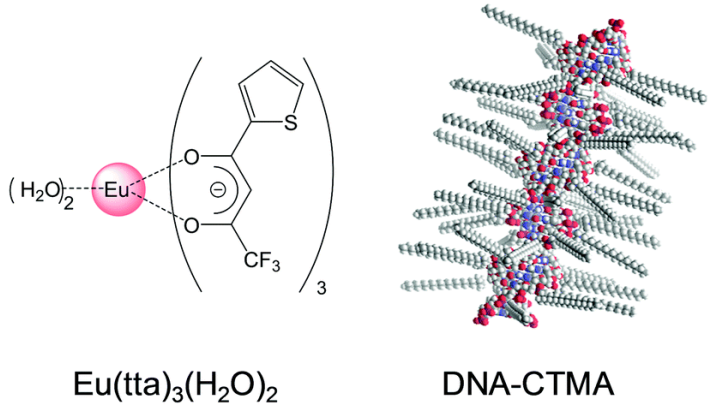

Figure 1-8 The chemical structure of $Eu(tta)_3(H_2O)_2$ and a schematic drawing of DNA–CTMA.

1.2 Luminescent hybrid material based on clay

Clay is abundant in mineral storage resources worldwide, characterized by its low cost and excellent properties, including adsorption, swelling, ion exchange, suspension, dispersion, and binding capabilities. After modification, clay exhibits significantly improved dispersion and adsorption abilities, making it suitable as an additive in the polymer materials industry, particularly in rubber and plastics. It enhances the mechanical properties of polymers, including impact resistance, fatigue resistance, thermal stability, flame retardancy, and barrier properties, while also improving the processing characteristics of polymers. Additionally, clay serves as an adsorbent for toxic substances, a coating agent, and a catalyst. Consequently, it is highly favored in society and has been lauded as a "universal material."

1.2.1 Concepts of clay

Layered clay minerals have garnered extensive research attention as host matrices capable of encapsulating chemical substances without altering their properties. This interest stems from the distinctive properties of layered clay minerals, including their strong adsorption capacity, high interlayer ion exchange ability, and structural adaptability, which enable the incorporation of various interlayer species. Additionally, their inherent chemical inertness, exceptional stability, and widespread availability make them highly advantageous[81, 82]. Within these minerals, atoms in the layers are bonded through stable covalent interactions, while the interlayer space is stabilized by weaker forces such as electrostatic attraction, π-π stacking, and other secondary bonding interactions. This structural arrangement allows for the encapsulation and retention of ionic materials or complex compounds within the interlayer space without compromising the integrity of the layered framework[83]. The insertion of cations can selectively target specific exchangeable cation sites within the clay mineral interlayers, facilitating the quantitative and dispersed incorporation of cationic materials, resulting in stable hybrid materials with enhanced properties[84].

Kaolinite[85-88] and montmorillonite[83, 89] are among the most commonly utilized layered clay mineral matrices. Clay minerals are generally categorized into two types—1:1 and 2:1—based on variations in their unit layer structures (**Figure 1-9**). Kaolinite is a typical 1:1 type (TO) clay mineral composed of a silica tetrahedral layer (T) and an aluminum octahedral layer (O). Due to the minimal lattice substitution in its structure, kaolinite exhibits relatively poor ion exchange capacity. Kaolinite features two distinct interlayer surfaces: Si–O and Al–OH. The presence of abundant hydroxyl groups within the interlayers enables the covalent grafting of reactive functional groups onto kaolinite.

In contrast, montmorillonite belongs to the 2:1 (TOT) clay mineral category and exhibits significant lattice substitution, leading to a high concentration of exchangeable cations in its interlayer space.

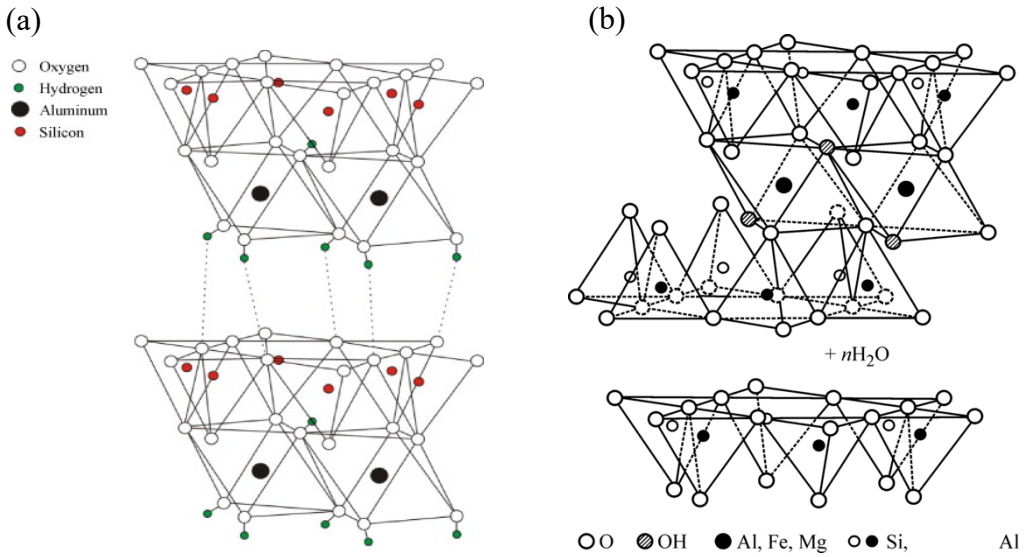

Figure 1-9 The structure of (a) kaolinite (1:1-type) [90] and (b) montmorillonite (2:1-type) [91]

By analyzing the structure and properties of clay minerals, methods for preparing lanthanide complex/layered clay mineral hybrid luminescent materials primarily involve the ion exchange of Eu^{3+} ions into the interlayer spaces of the clay minerals, followed by the addition of ligands to synthesize lanthanide element complexes in situ within the interlayers[92, 93]. This approach has been extensively studied. Additionally, methods that involve the reaction of active functional groups of ligands with the -OH groups of clay minerals, followed by the covalent grafting of lanthanide complexes onto the clay minerals, have also been widely investigated[94]. However, there is limited research on the direct doping of lanthanide complexes with layered clay minerals, particularly regarding the interactions and mechanisms associated with varying ratios of the two materials.

1.2.2 Incoparating Eu(III) complex into clay minerals

Despite the advantages of rare earth luminescent complexes, such as high luminous efficiency, long fluorescence lifetime, and high emission purity, they often exhibit poor thermal, optical, chemical stability, and mechanical processing properties. Layered clays typically provide flexible interlayer spaces that can accommodate guest species, acting as an intermediary between two "hard" layers and adapting to a certain extent to

the size of the guest. In recent decades, luminescent clay-based hybrid materials, formed by incorporating lanthanide complexes into clay matrices, have advanced significantly. These materials retain the distinctive optical characteristics of lanthanide complexes, including sharp emission lines, prolonged decay times, and large Stokes shifts, while also leveraging the benefits of the clay matrix, such as high stability, optical transparency, tunable colors, and facile surface functionalization[95].

Attapulgite is a naturally occurring stable mineral with a layered chain structure, known for its large specific surface area and exceptional adsorption properties. Ma et al. employed 3-aminopropyltriethoxysilane (APTES) as a coupling agent to establish covalent linkages between organic guest molecules and the inorganic matrix[96]. Subsequently, they covalently grafted the europium complex $Eu(TTA)_3(H_2O)_2$ onto the external surface of attapulgite via ligand exchange reactions (**Figure 1-10**). This represents the first instance of covalently grafting a lanthanide complex onto clay minerals, providing a novel approach for the preparation of lanthanide complex hybrid luminescent materials. The resulting hybrid luminescent materials emit bright red light under ultraviolet irradiation and demonstrate high thermal stability and resistance to photodegradation. Additionally, the attapulgite-based europium complex exhibits excellent properties, including high luminescent efficiency, long fluorescence lifetime, and low cytotoxicity, making it valuable for applications in cellular imaging and as biological markers[97-100].

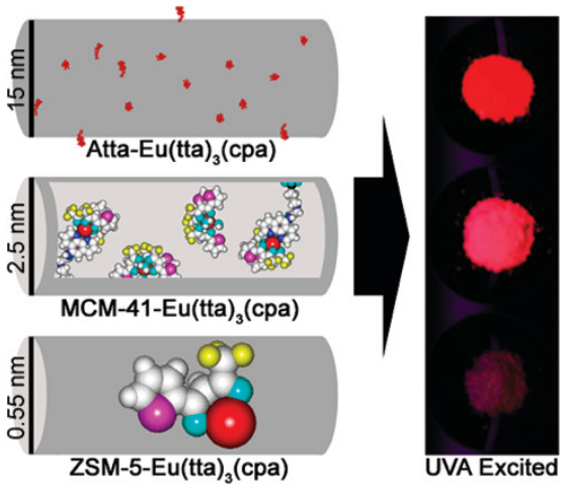

Figure 1-10 Predicted structure of $Eu(tta)_3(cpa)$ with various matrix (Atta, MCM-41 and ZSM-5). The photograph displays the composites under UV irradiation at 365 nm.

Kaolinite is a layered aluminum silicate clay mineral belonging to the 1:1 type[101, 102]. Hydroxyl groups are present between the layers of kaolinite, allowing for the

covalent grafting of luminescent organic complexes through condensation reactions. Research by Faria et al. demonstrated the covalent grafting of pyridine-2-carboxylic acid onto kaolinite (Ka-pa)[103]. A certain amount of Ka-pa was dispersed in an ethanol solution containing Tb^{3+}, where Tb^{3+} coordinated with oxygen and nitrogen atoms through coordinate bonds (denoted as Tb(Ka-pa)). Acetylacetone (ACAC) was employed as a secondary ligand to enhance Tb^{3+} sensitization, yielding a layered hybrid luminescent material, Tb(Ka-pa)(ACAC, as shown in **Figure 1-11**. This hybrid material demonstrated stronger green luminescence and improved thermal stability compared to the pure complex. Additionally, Araujo et al. replaced pyridine-2-carboxylic acid with 2,6-pyridine dicarboxylic acid as a ligand, incorporating it into kaolinite layers via a soft guest method[87]. The presence of two carboxyl groups in 2,6-pyridine dicarboxylic acid enhances its coordination ability, enabling the hybrid material to retain excellent luminescent properties even in the absence of a secondary ligand.

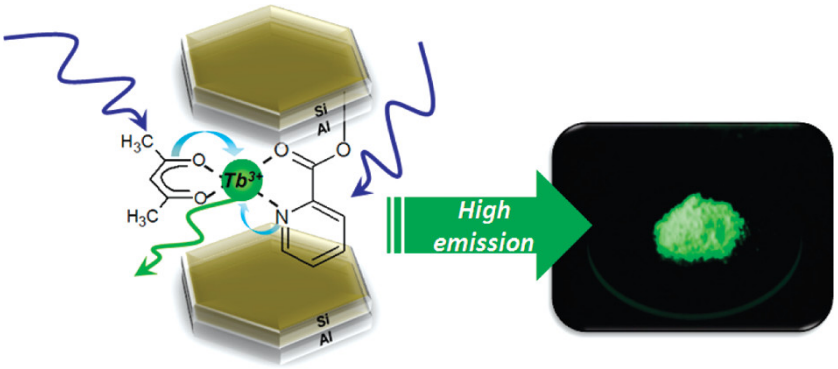

Figure 1-11 Scheme of the preparation of luminescent hybrid materials (Tb(Ka-pa)(ACAC) based on kaolinite with photographs under near UV-light illumination.

Among various matrix materials, montmorillonite minerals are regarded as highly promising. With a large specific surface area and strong retention capacity within its interlayer spaces, montmorillonite facilitates the intercalation of complexes through electrostatic interactions or ion exchange processes. This incorporation enhances the thermal, chemical, and mechanical stability of the complexes. Ryu et al. successfully intercalated europium(III) complexes into Na^{+}-montmorillonite, forming a hybrid material with outstanding luminescent properties and high stability, making it suitable for applications such as fluorescent fingerprint detection and identification[104]. Yang et al. synthesized europium-clay hybrid materials ($Eu^{3+}(TTA_n)$@Lap) on synthetic montmorillonite (Laponite) nanodisks through an ion exchange method (**Figure 1-12**)[105]. Surprisingly, the luminescent efficiency of $Eu^{3+}(TTA_n)$@Lap was significantly

enhanced upon the addition of ionic liquid to its aqueous solution, with the absolute quantum efficiency increasing from 0.1 to approximately 0.7. This represents a notably high value rarely observed in luminescent hybrid materials under aqueous conditions.

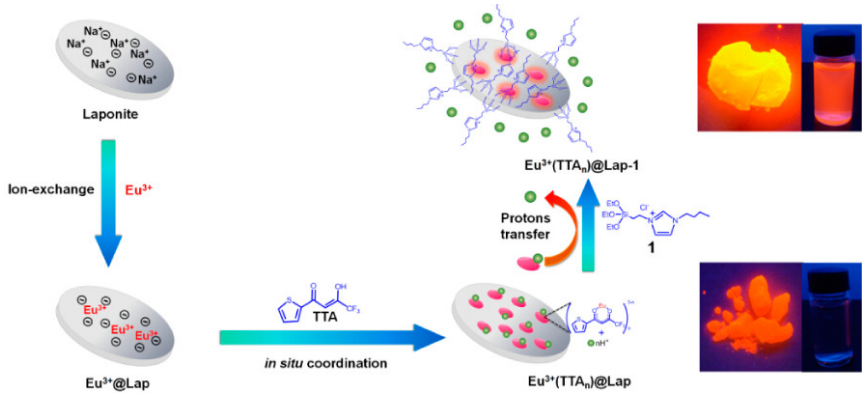

Figure 1-12 Fabrication process of the luminescent hybrid material ($Eu^{3+}(TTA_n)$@Lap) with photographs under UV-light illumination.

Fluorescent sensors can be developed using clay-based hybrid materials. Chen et al. discovered that the hybrid material $Eu(DPA)_3$@Lap-Tris (where DPA = pyridine-2,6-dicarboxylic acid, Lap = Laponite, and Tris = tris(hydroxymethyl)aminomethane) exhibits selective recognition of glutathione (GSH) in solutions or hydrogels through a "switching" mechanism[106]. As shown in **Figure 1-13,** Cu^{2+} quench the luminescence of $Eu(DPA)_3$@Lap-Tris via photoinduced electron transfer (PET). However, upon the introduction of GSH, Cu^{2+} are removed, effectively restoring (switching on) the luminescence of $Eu(DPA)_3$@Lap-Tris, demonstrating both high selectivity and sensitivity. Li et al. recently reported a simple and effective luminescent sensor for detecting cationic surfactants[107]. They constructed the luminescent sensor, denoted as Eu^{3+}(TTAn)@Lap, by intercalating luminescent Eu^{3+}(TTAn) into the interlayers of Laponite clay. Contact with cationic surfactants in aqueous solutions, such as cetyltrimethylammonium bromide (CTAB), significantly enhances its luminescence. In contrast, other types of surfactants do not notably affect the sensor's luminescence. Therefore, Eu^{3+}(TTAn)@Lap can be used to differentiate between cationic surfactants and other types of surfactants. Chiang et al. developed a novel lanthanide-containing PG/PDA/Tb^{3+}@Lap nanocomposite material. Compared to the PG/PDA hydrogel, the PG/PDA/Tb^{3+}@Lap nanocomposite hydrogel exhibits smaller pore sizes, higher mechanical strength, and lower swelling rates[108]. The presence of reversible dynamic bonds in the PG/PDA/Tb^{3+}@Lap hydrogel imparts shear-thinning behavior, self-healing capabilities, and injectability, enabling its processing through electrospinning

and 3D printing to accommodate diverse structural requirements. Additionally, the PG/PDA/Tb^{3+}@Lap hydrogel can also function as a luminescent sensor for the detection of Cu^{2+} in a concentration range of 1×10^{-6} to 1×10^{-3} M, demonstrating good selectivity and sensitivity.

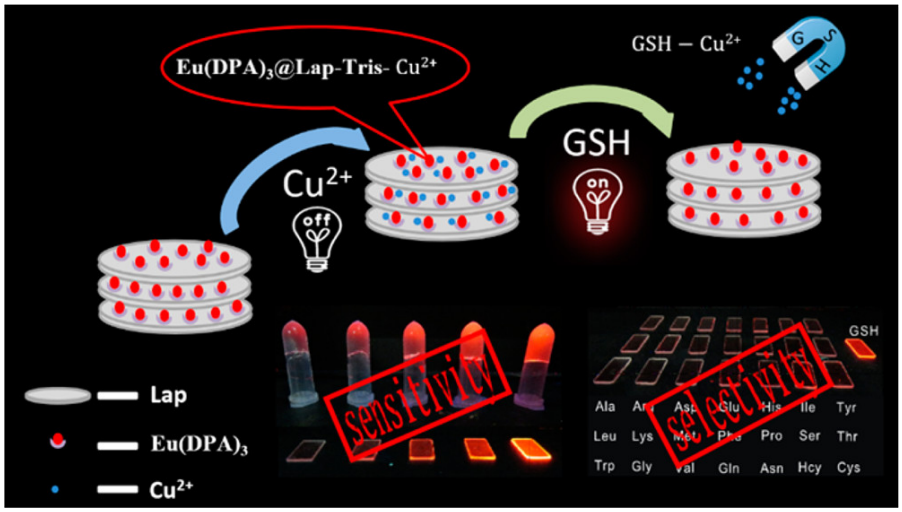

Figure 1-13 Diagrammatic illustration of $Eu(DPA)_3$@Lap-Tris preparation and GSH detection.

1.3 Electrochromic (EC) and Electrofluorochromic (EFC) of luminescent hybrid material

Materials are the foundation of production and daily life, and those that can identify changes in the external environment and alter their inherent physical or chemical properties in response are ideal choices for the development of future "smart manufacturing." When subjected to external stimuli, these materials can change their shape, color, transparency, or other properties and functionalities. Such changes significantly enhance the materials' adaptability to their environment, making them key to addressing future societal challenges. As a type of multifunctional smart material, stimuli-responsive materials can modulate their optical properties, such as emission and coloration, and have found widespread applications in various fields, including displays, memory storage, security, and biological probes[109, 110]. The reversible switching of the optical characteristics of stimuli-responsive materials can be controlled by various external stimuli, such as electric fields, temperature, light, mechanical force, and solvents or vapors[111, 112]. Among these external stimuli, electric fields are particularly significant due to their ease of operation, cleanliness, precision, and ability to achieve rapid responses. By controlling the electric field, it is possible to precisely adjust the

optical properties of stimuli-responsive materials, making them important in applications such as display technology, data storage, and sensors. The intelligent characteristics of these materials not only enhance their functionality but also provide new ideas and methods for addressing the complex challenges faced by society today. The research and application of stimuli-responsive materials are expected to promote the development of smart manufacturing, encourage efficient and environmentally friendly production methods, and ultimately contribute to sustainable societal development.

1.3.1 What's the Electrochromic (EC)

Electrochromic materials typically consist of two components: a luminescent entity and an electroactive unit, connected through co-polymerization, hybridization, or covalent bonding. The luminescence intensity or color of these materials can be reversibly modulated via electrochemically driven redox reactions. This luminescence switching property allows for in situ and simultaneous detection of electrochemical and photophysical signals, facilitating a deeper understanding of chemical reactions, electron transfer, and other processes. In 1993, Lehn et al.[113] reported the first example of an electroluminescent electrochromic material, created by combining a bipyridine ligand metal Ru(II) complex with an electroactive quinone group, resulting in a material that exhibited distinct luminescence properties upon electrical stimulation.

Electrochromic mechanism

Electrochromism is a unique property of materials, wherein luminescence can be modulated by applying an external voltage. The electroluminescent chromic behavior of these materials primarily stems from four mechanisms: (a) modulation of electron or proton transfer between the redox-active component and the luminescent species, a process referred to as the photoinduced electron transfer (PET) effect[114]; (b) energy transfer mechanisms, such as Förster resonance energy transfer (FRET)[115] and Dexter energy transfer[116]; (c) altering the luminescent properties by adjusting the redox state of the electroactive luminescent component; and (d) ionic migration among luminescent ions.

For conjugated or non-conjugated multicomponent materials, they consist of redox-active units and a luminescent entity connected through various methods, often involving mechanisms of PET and FRET. Under electrical stimulation, the electrochemical reactions induced by the redox-active units influence the PET or FRET processes, leading to changes in the emission characteristics of the luminescent entity. This process can be controlled by reversibly modifying the oxidation state of the redox

units, as depicted in **Figure 1-14(a)** and **Figure 1-14(b)**. Another key mechanism responsible for photoluminescence quenching in binary component materials is energy transfer. The two most commonly observed energy transfer mechanisms are FRET and Dexter energy transfer. The FRET process is primarily governed by the spectral overlap between the absorption spectrum of the redox-active units and the emission spectrum of the luminescent species[117]. Applying an external electric field can alter the absorption band of the electroactive units, thereby changing the overlapping region with the emission band of the luminescent entity. Consequently, the efficiency of the FRET process can be adjusted, affecting the emission characteristics of the electroluminescent chromic material system. In contrast to FRET, the Dexter energy transfer process requires orbital overlap between the fluorophore and the quencher, where electron transfer occurs, transferring the photonic excitation energy from the donor to the acceptor unit at shorter microscopic distances[118].

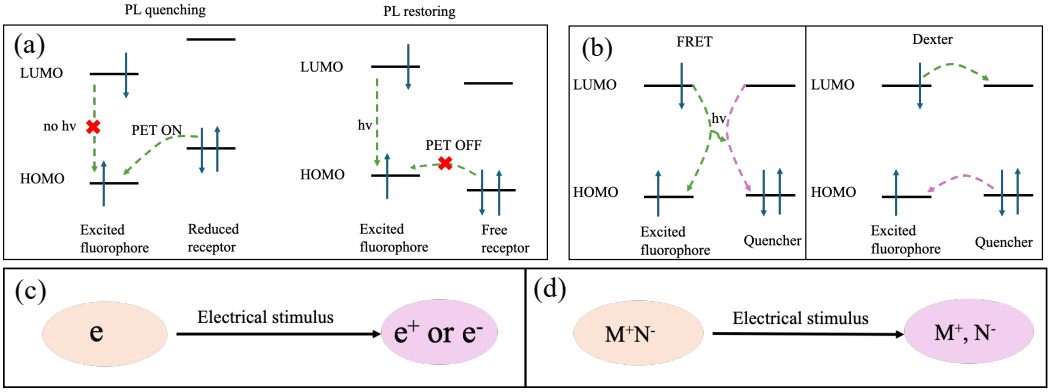

Figure 1-14 Four mechanisms of electroluminescent color change behavior: (a) PET; (b) Förster resonance energy transfer (FRET) and Dexter energy transfer; (c) redox state of electroactive luminophores; (d) ion migration between ionic luminophores.

For single-component electroresponsive luminescent entities, reversible oxidation or reduction reactions can occur under electrical stimulation, resulting in changes to the emission characteristics of the material, as depicted in **Figure 1-14(c)**. Ionic migration is also a significant mechanism for regulating the electroluminescent chromic behavior of materials (**Figure 1-14(d)**), primarily applied in ionic luminescent entities. In materials such as metal complexes, cationic metal complexes interact with anions through non-covalent interactions like hydrogen bonding. Under electrical stimulation, ionic migration occurs in the material within a solution, affecting the non-covalent interactions and subsequently altering the electron cloud density and the HOMO-LUMO energy gap of the ionic luminescent entities, thereby resulting in changes in the emission wavelength. On the other hand, the migration of anionic and cationic

components in the luminescent entity to the anode and cathode, respectively, under an applied electric field leads to different electroluminescent chromic phenomena. Currently, the mechanisms of electroluminescent chromism in the developed materials can be categorized into these four types.

1.3.2 What's the Elecfluotrochromic (EFC)

Over the past decade, the interdisciplinary field of "luminescence and electrochemical coupling" has attracted significant interest. Electroluminescent chromism, a key physicochemical phenomenon in this domain, enables reversible modulation of photoluminescence through the application of an electric potential. This distinctive behavior arises from the electrochemical reactions of photoelectrochemical functional materials. Fluorochromic functional materials, including molecules[119], metal complexes[120], conjugated polymers[121], and inorganic compounds[122, 123], can generally be classified into two main categories. As shown in **Figure 1-15**, the first class consists of materials that rely on intrinsic electrochemical properties, while the second class includes those that achieve chromic behavior through external stimuli or modifications in their molecular structure.

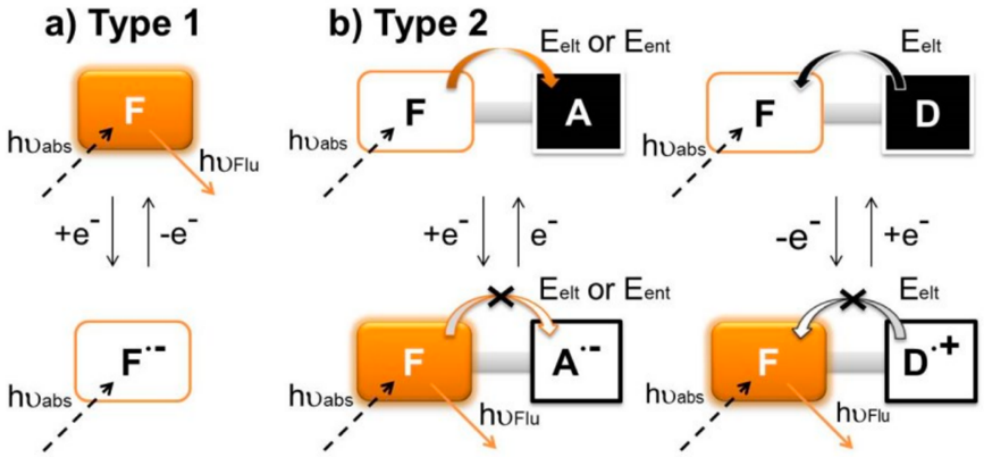

Figure 1-15 Electrochemical photoswitching systems (E_{elt}: electron transfer, E_{ent}: energy transfer).

Elecfluotrochromic mechanism

When the luminescent core undergoes electrochemical redox reactions, its photoluminescence intensity and wavelength can be modulated by applying an external potential, which drives these redox processes. Electroluminescent chromism materials and devices operating via this mechanism are classified as Type 1. In this category, luminescent properties are directly governed by redox reactions, leading to the

generation of oxidized/reduced ions and free radicals. The electronic states of the luminescent molecules are directly influenced by the electrochemical processes. As a result, the energy gap between the excited and ground states, which determines the luminescence wavelength and quantum yield, is often markedly influenced. The electroluminescent chromism reaction of derivatives is a typical example of Type 1 materials[124-126]. Upon electrochemical reduction, the yellow photoluminescence of neutral tetrazine molecules is effectively quenched, as the reduced form—its anionic radical—lacks luminescent properties. Consequently, electrochemical devices incorporating these materials can be readily constructed by positioning a mixed solution between two opposing transparent electrodes.

To expand luminescence modulation to a broader range of luminescent molecules, including those lacking inherent redox activity, researchers have investigated electrochemically controlled electron or energy transfer mechanisms. In this strategy, the luminescent core is conjugated with a redox-active segment that acts as a luminescence quencher through photoinduced electron or energy transfer between the excited luminescent species and the redox-active component. This type of luminescence modulation, driven by redox reactions in the external segment, is categorized as Type 2. Since luminescence modulation in Type 2 materials results from electron or energy transfer between the fluorophore and an external switching component, its properties differ from those of Type 1. In Type 2, the effectiveness of photoluminescence switching is primarily governed by the efficiency of electron or energy transfer between the fluorophore and the external switching segment.

1.3.3 Electroswithchable optical device containing Eu(III) complex

We investigated the electroluminescent chromism reactions of luminescent lanthanide (III) complexes, which belong to the Type 2 mechanism. The electrochemical regulation of photoluminescence can be achieved through intramolecular energy transfer from the lanthanide (III) complexes to the electroluminescent chromic molecules. In our study, by combining photoluminescent materials with electroluminescent chromic compounds, we were able to utilize the redox reactions of the chromic materials to control the energy transfer between the two types of materials.

As illustrated in **Figure 1-16**, when the electroluminescent chromic compound is in a transparent, colorless state (i.e., lacking electronic transition bands in the visible to near-infrared region), the energy gap between its ground and excited states exceeds that of the luminescent compound emitting in the visible spectrum. In this state, energy transfer from the photoluminescent material to the electroluminescent chromic

compound is negligible, allowing the luminescence of the photoluminescent species to be observed, resulting in an "emission mode." Conversely, as a result of electrochemical reactions, the energy gap of the electroluminescent chromic material becomes narrower than that of the photoluminescent material. In this chromatic state, the excitation energy of the luminescent species can be transferred to the colored electroluminescent chromic material. This energy transfer primarily occurs via Förster resonance energy transfer (FRET), which is driven by Coulombic interactions between the energy donor and acceptor. Effective FRET-based luminescence modulation requires significant spectral overlap between the donor's emission and the acceptor's absorption. Since this energy transfer quenching results in the suppression of photoluminescence, only the coloration of the electroluminescent chromic material can be observed, while the photoluminescence becomes undetectable, leading to a "reflection mode."

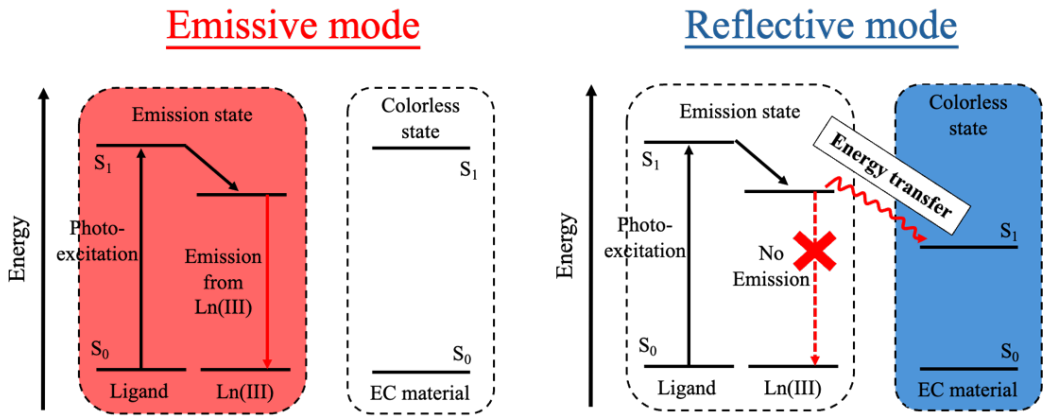

Figure 1-16 Energy diagrams of the dual-mode material based on EC material and luminescent Ln(III) complex. The left diagram illustrates the emissive mode, while the right diagram depicts the reflective mode of the dual-mode system.

We incorporated red-emitting Eu(III) complexes and electrochromic viologen molecules into an electrolyte solution, sandwiching them between two ITO electrodes. By employing electrochemical methods to modulate photoluminescence and absorption, we successfully developed a dual-electrode electrochemical device[127]. As shown in **Figure 1-17**，in the open-circuit state, the device exhibits fluorescence under UV light, which we define as the 'emission state.' When a voltage is applied, the fluorescence of the Eu(III) complexes is quenched, while the electrochromic molecules induce a color change in the solution from colorless to cyan. Electrochemical analysis revealed that the fluorescence intensity and lifetime of the electrolyte solution containing only the Eu(III) complex remained unchanged upon voltage application. This suggests that the

emission modulation in the Eu(III) complex/HV^{2+} solution is primarily influenced by the presence of the colored HV^{2+} species. The photochemical and electrochemical properties of the hybrid material demonstrate that the photoluminescence modulation originates from energy transfer between the excited Eu(III) complex and the colored viologen species. We have successfully achieved electrochemical control of photoluminescence synchronized with color change by utilizing the concept of "emission control based on electrochromic reactions".

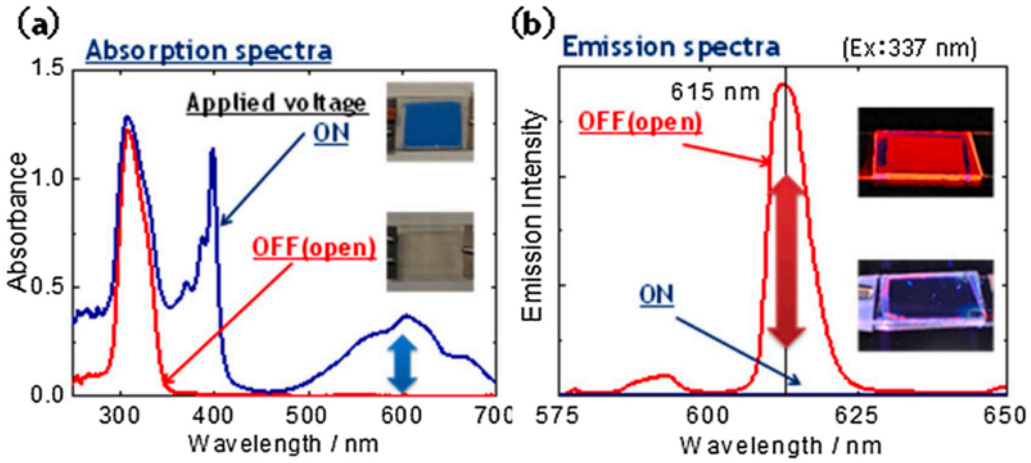

Figure 1-17 (a) Absorption spectra of the dual mode device based on EC viologen molecule and Eu(III) complex under open circuit condition and colored states (− 2.2 V). (b) Photoluninescence spectra of the electrichemical device under open circuit condition and colored states (–2.2 V), with an excitation wavelength of 337 nm.

Then, we used an electrofluorochromic device to demonstrate bimodal representation. A prototype electrofluorochromic device with numerical display capabilities was constructed by placing an electrolyte solution containing $Eu(hfa)_3(H_2O)_2/HV^{2+}$ between a seven-segment patterned ITO electrode and a planar ITO electrode[128]. As illustrated in **Figure 1-18**, upon applying a coloring voltage to HV^{2+} in a specific segment, the material transitions from a colorless, transparent state to cyan due to the electrochromic reaction of viologen. This electrochromic effect enables numerical representation in reflection mode. Conversely, when the device is exposed to ultraviolet light, the Eu(III) complex undergoes photoexcitation, emitting strong red luminescence from all segments except the colored area. This results in an emissive display of numerical

characteristics. Based on this approach, bimodal representation has been successfully demonstrated.

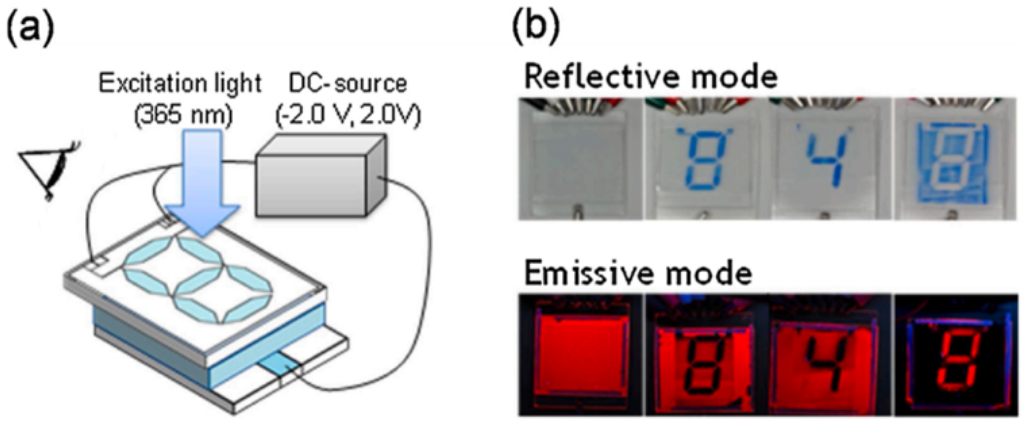

Figure 1-18 (a) Schematic illustration of the seven-segment dual-mode device. (b) Photographs depicting the device's representations in both reflective and emissive modes, enabling clear visual recognition of numerical expressions.

For a rapid electroluminescent response, immobilizing both functional materials on the same electrode is essential, as this strategy minimizes the time required for electrochemical reactions. In such immobilized systems, the fluorescence of functional molecules and ions is primarily governed by the Förster resonance energy transfer (FRET) mechanism. We modified porous titanium dioxide (TiO_2) electrodes with viologen and Eu(III) complexes to prepare bifunctional TiO_2 electrodes[129]. Through electrochemical reactions, we successfully achieved rapid modulation of red photoluminescence while simultaneously inducing the coloring and bleaching of viologen derivatives. Based on luminescence lifetime and quantum yield measurements, the underlying mechanism of this modulation is attributed to electron transfer between the Eu(III) complex and TiO_2, as well as interactions between the Eu(III) complex and the reduced viologen species. This bifunctional electrode demonstrated an exceptional response time (<5 s) and high cycling stability (>150 cycles), enabling the simultaneous modulation of both luminescence and color.

Chapter 2

Enhanced Photoluminescence Performance of Eu(III) Complex Hybridized with Smectite

Chapter 2 Enhanced Photoluminescence Performance of Eu(III) Complex Hybridized with Smectite

As introduced in Chapter 1, smectite as multilayered inorganic materials, possess distinctive characteristics that offer quasi-two-dimensional spaces, rendering them intriguing microenvironments for chemical reactions (**Figure 2-1(a)**). Recently, synthetic clay minerals have garnered significant attention for their potential applications in photochemical reactions involving various types of dyes. Materials derived from Eu(III) complexes integrated with smectite exhibit considerable potential across diverse applications owing to their precisely controlled purity, multifunctional properties, as well as mechanical, thermal, and chemical stabilities, coupled with biocompatibility. Several studies have employed ion exchange reactions to intercalate Eu^{3+} ions between clay layers for the fabrication of luminescent hybrid materials. However, the dispersibility of this luminescent hybrid material in solution is poor, resulting in low transparency of the solution, which limits its potential applications. Furthermore, research on the interaction and photophysical properties between the Eu(III) complex and smectite without ion-exchange reactions is not comprehensive.

In this study, the emission properties of Eu(III) complex hybridized with smectite were studied. Smectite was employed with intercalated functional groups (methyltri-n-octylammonium ion) between its layers to ensure effective dispersion in middle–high polar organic solvents. It was utilized in the fabrication of hybrid materials incorporating the Eu(III) complex (chemical structure of the Eu(III) complex is shown in **Figure 2-1(b)**). The Eu(III) complex/smectite hybrid solutions were prepared by mixing the Eu(III) complex and smectite, resulting in good transparent material dispersed solution. The photophysical properties of the Eu(III) complex in smectite solutions were examined both experimentally and theoretically. Furthermore, polymer was introduced into the Eu(III) complex/smectite hybrid solutions to fabricate the films via dip-coating and drop-coating methods. These hybrid films exhibited great transparency, smoothness, and luminescence performance. The results indicate that smectite not only improves the film-forming capabilities but also enhances the emission intensity of the Eu(III) complex film.

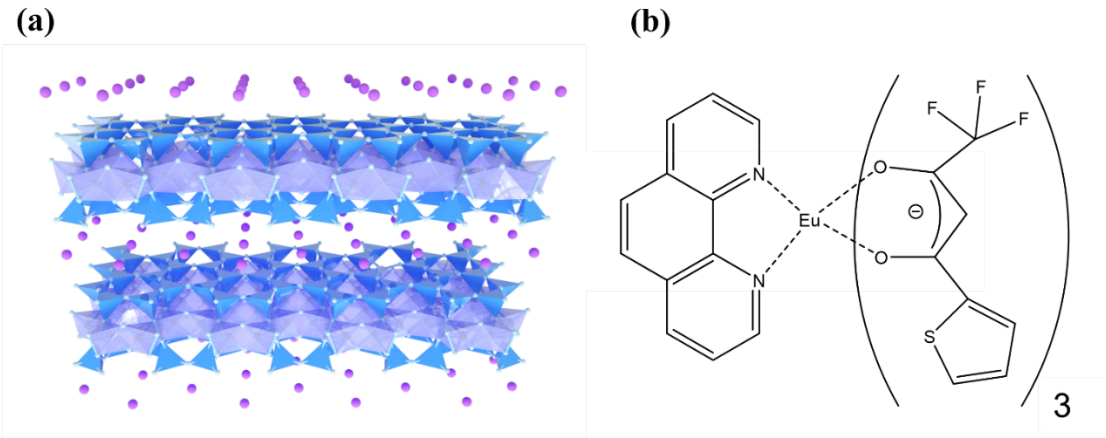

Figure 2-1 (a) Schematic of smectite and (b) chemical structure of Eu(tta)$_3$phen.

Preparation of Eu(tta)$_3$phen/smectite hybrid solutions

Eu(tta)$_3$phen/smectite solutions were prepared by mixing Eu(tta)$_3$phen and smectite in acetonitrile at room temperature. The concentration of Eu(tta)$_3$phen was maintained at a fixed value of 0.1 mmol/L. In each solution, the amount of Eu^{3+} was 2.0×10^{-3} mmol, and the cation exchange capacity of smectite ([clay]) ranged from 2.73×10^{-3} to 3.29×10^{-2} meq. Therefore, the ratio of the Eu(tta)$_3$phen and cation exchange capacity of smectite ([Eu^{3+}]:[clay]) varied from 1:0 to 1:16.4.

Preparation of Eu(tta)3phen/smectite/PMMA hybrid films

Glass substrates were cleaned using a special detergent, followed by rinsing with deionized water (twice) and ultrasonic cleaning with acetone for 20 min. The films were prepared using the drop-casting method, wherein 50 μL of the hybrid solution was dropped on a glass substrate and dried at room temperature. Another type of film was fabricated on the glass surface using dip–coating methods with pulling speed at 4 mm/s.

2.1 Photoluminescence performance of Eu(III) complex/smectite hybrid material in solution state

2.1.1 Photophysical properties of the Eu(tta)$_3$phen/smectite hybrid solutions

The preparation of the mixed luminescent material involving Eu(III) complexes within the layers of smectite was achieved using a direct mixing method. The absorption spectra of the Eu(tta)$_3$phen/smectite hybrid materials, recorded between 200 and 450 nm in the solution, are shown in **Figure 2-2 (a)**. The absorption bands at approximately 271 and 340 nm are attributed to π–π* transitions of the phen and tta

ligands, respectively[130]. Compared with pure Eu(tta)$_3$phen, the blue-shifted tta and phen ligands indicate that the structure of Eu(tta)$_3$phen is distorted by the microenvironments of smectite. With an increase in the smectite content, the absorption peak at 271 nm decreases, and that of a new absorption at 263 nm increases. An isosbestic point appears at 266 nm, and the absorption bands at longer and shorter wavelengths from the isosbestic point correspond to the two states of Eu(tta)$_3$phen before and after the interaction, respectively. **Figure 2-2 (b)** shows relationship between absorbance (263 and 271 nm) and smectite content. When the smectite content exceeds [Eu^{3+}]:[clay] = 1:4.1, the change in the absorbance at 271 and 263 nm is gradually saturated, indicating that almost all the existing Eu(III) complexes have interacted with smectite. The absorption of the ligand at 340 nm is also slightly decreased with an increase in the smectite content. This reduction in the tta ligand absorption can be attributed to the weak perturbation of the chelating effect of the bidentate tta ligands, influenced by the steric effect of the planar smectite layers[131].

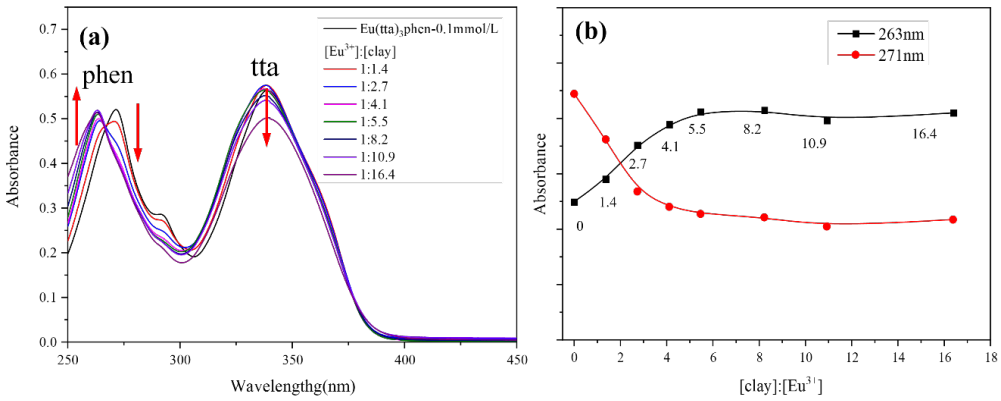

Figure 2-2 (a) Absorption spectra of ligands and Eu(tta)$_3$phen/smectite hybrid solutions; (b) absorbance change at 263 nm (black line) and 271nm (red line) of phen ligand.

To study the luminescence properties of the Eu(tta)$_3$phen/smectite hybrid materials after adding smectite, the emission spectra of the hybrid solutions were measured. **Figure 2-3(a)** shows the emission spectra of Eu(tta)$_3$phen/smectite in the acetonitrile solution with excitation at 340 nm. Specific sharp emission bands from Eu(III) complexes are observed at wavelength from 550 to 750 nm with characteristic $^5D_0 \rightarrow {}^7F_J$ transitions for J = 0-4, leading to a red emission. The most intense band of $^5D_0 \rightarrow {}^7F_2$ transition at 612 nm resulting from the induced electric dipole character is known

as the hypersensitive emission band to the coordination environment[132]. In the solution state, the luminescence intensity of the $^5D_0 \rightarrow {}^7F_2$ transition solution first increases and then decreases with an increase in the amount of clay, reaching the maximum at $[Eu^{3+}]$:[clay] = 1:4.1 (**Figure 2-3(b)**). Interestingly, the shapes of the emission peaks assigned to the $^5D_0 \rightarrow {}^7F_2$ (**Figure 2-3(c)**) and $^5D_0 \rightarrow {}^7F_4$ (**Figure 2-3(d)**) transitions change after adding smectite.

Both transitions are induced by the ED transition. Therefore, the shapes of the luminescence bands are also affected by the structure surrounding Eu^{3+} ions, with significant spectral variations observed in the presence of smectite. This suggests that the ligand field of $Eu(tta)_3phen$ is perturbed due to its interaction with smectite.

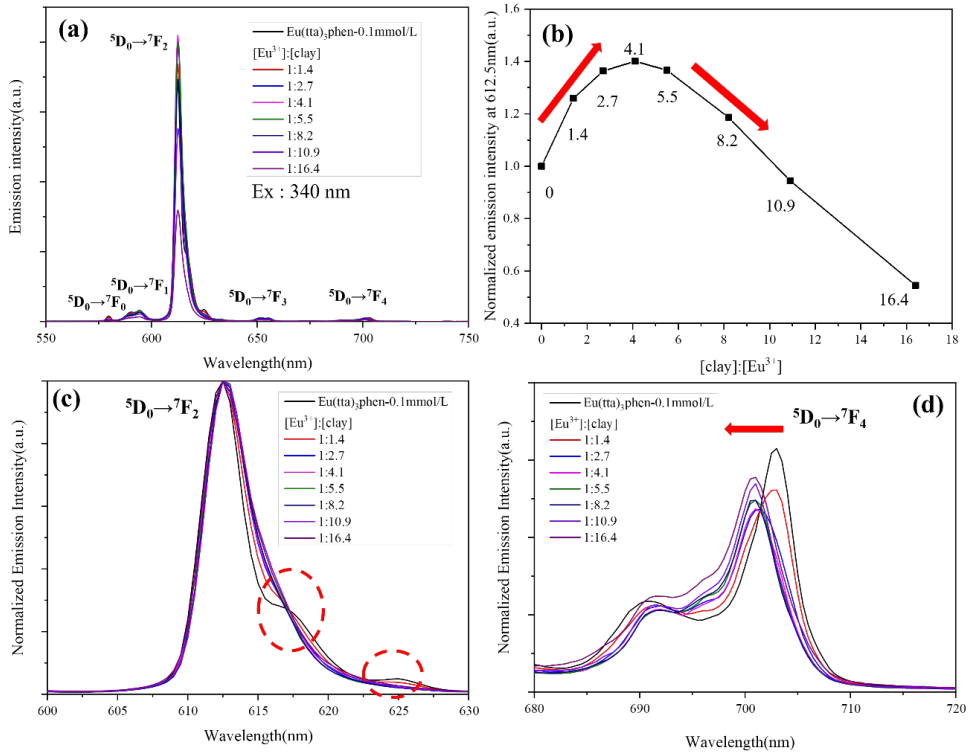

Figure 2-3 (a) Emission spectra of $Eu(tta)_3phen$ and $Eu(tta)_3phen$/smectite hybrid solutions; (b) normalized emission intensity at 612.5 nm with the ratio of [clay]:$[Eu^{3+}]$ from 0:1 to 16.4:1. Expanded emission spectra of the $Eu(tta)_3phen$/smectite hybrid solutions for (c) $^5D_0 \rightarrow {}^7F_2$ and (d) $^5D_0 \rightarrow {}^7F_4$ transitions. Excitation wavelength is 340 nm.

Normally, Eu^{3+} with a highly symmetrical ligand field rarely exhibits strong emission owing to the low radiative rate resulting from its high symmetry[133]. For the present Eu(III) complex, the emission peak corresponding to the $^5D_0 \rightarrow {}^7F_2$ transition near 612

nm is due to ED. By contrast, the emission peak of the $^5D_0 \rightarrow {}^7F_1$ transition is mainly due to the magnetic dipole (MD), which is not significantly affected by the ligand field. Thus, the symmetry of the Eu(III) complex can be estimated from the ratio of the emission intensities derived from the MD (I_{MD}) and the ED (I_{ED})[134].

A low Irel value ($I_{rel} = I_{ED} / I_{MD}$) indicates a high symmetry occupied by the Eu^{3+} sites. As shown in **Figure 2-4**, the Irel value increases from 13.0 ([Eu^{3+}]:[clay] =1:0) to 15.1 ([Eu^{3+}]:[clay] =1:4.1) with an increase in the smectite content and then decreases to 11.6 ([Eu^{3+}]:[clay] =1:16.4). This result indicates that the symmetry of the coordination environment of $Eu(tta)_3phen$ is influenced by the interaction with smectite. the symmetry of Eu^{3+} is the lowest, and the f-f transitions are more allowed, resulting in the highest luminous intensity[135]. The low symmetry leads to more pronounced energy level splitting, which increases the emission lines of Eu(III) complex and leads to the broadening of luminescence band due to overlapping several emission lines, further corroborating the observed broadening of the emission spectra.

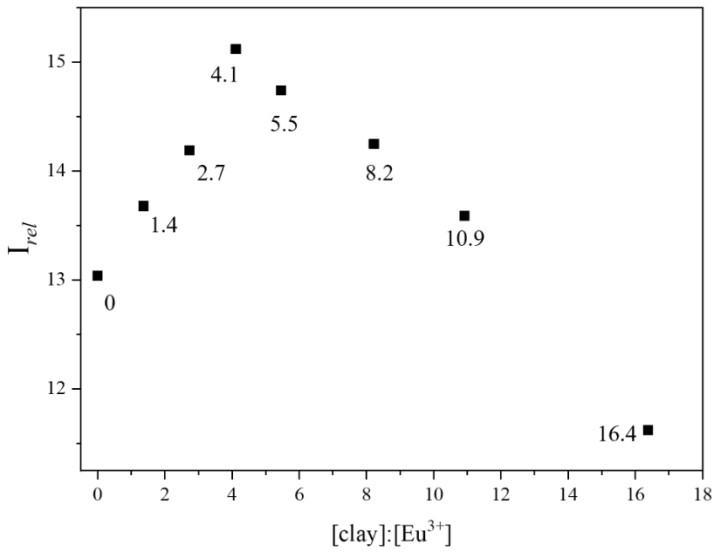

Figure 2-4 I_{rel} values with the ratio of [clay]:[Eu^{3+}] from 0:1 to 16.4:1 (relative intensities of $^5D_0 \rightarrow {}^7F_2$ transition (612 nm) to $^5D_0 \rightarrow {}^7F_1$ transition (590 nm)).

2.1.2 Interaction between Eu(tta)$_3$phen and smectite

Smectite improves the luminescence properties of Eu(III) complex, and we further studied the interaction between the Eu(III) complex and semctite. Following this, the states of the Eu(III) complex in the hybrid solution were elucidated. As presented in **Table 1** and **Figure 2-5(a)**, the lifetime decay curve for the pure Eu(tta)$_3$phen and Eu(tta)$_3$phen/smectite hybrid solutions with low smectite content can be fitted by a single exponential function, indicating the presence of only one luminescent component of the Eu(III) complex[136]. When [Eu^{3+}]:[clay] =1:10.9 and 1:16.4, the lifetime decay curves can be fitted by bi-exponential functions; a longer lifetime component (τ_2) appears and the contribution increases. The appearance of τ_2 indicates the coexistence of two different luminescent environments of Eu(III) complexes[137].

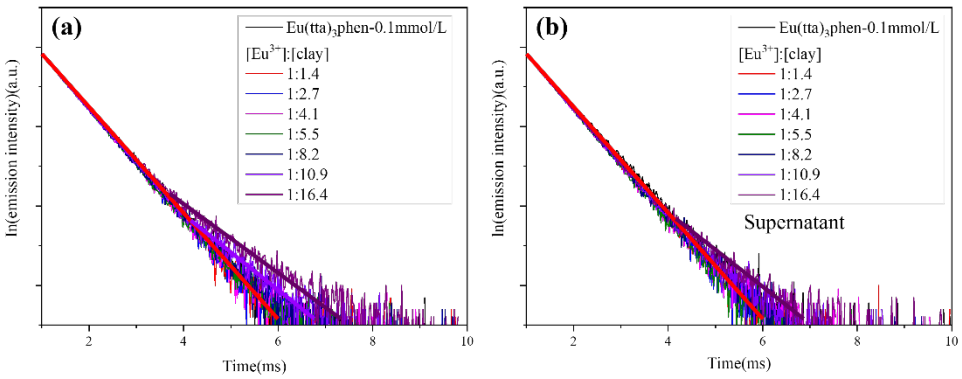

Figure 2-5 (a) The emission decay profiles of pure Eu(tta)$_3$phen and Eu(tta)$_3$phen/smectite hybrid solutions were analyzed. The profiles were fitted using single exponential (red line ([Eu^{3+}]:[clay] =1:0–1:8.2)) and bi-exponential functions (purple ([Eu^{3+}]:[clay] =1:10.9) and brown line ([Eu^{3+}]:[clay] =1:16.4)); (b) Emission decay profiles of pure Eu(tta)$_3$phen and supernatants were also analyzed. The profiles were fitted using single exponential (red line([Eu^{3+}]:[clay] =1:0–1:10.9)) and bi-exponential functions (brown line([Eu^{3+}]:[clay] =1:16.4))). The excitation wavelength was 340 nm.

To verify whether the Eu(III) complex is adsorbed in clay, the absorption spectrum of the supernatant after centrifugation of the hybrid solution was measured. When the clay content is low ([Eu^{3+}]:[clay] from 1:0 to 1:8.2), the absorbance of the supernatant and the hybrid solutions (original, before centrifugation) are almost unchanged (**Figure 2-6**). This indicates that almost no Eu(III) complex precipitates with the clay. However,

when [Eu^{3+}]:[clay] is 1:10.9 and 1:16.4, the absorbance of the supernatant decreases. This result shows that part of the $Eu(tta)_3phen$ complexes adsorbed on clay surface via various types of interactions, including polar or Coulombic forces, hydrogen bonding, and Van der Waals interactions[94].

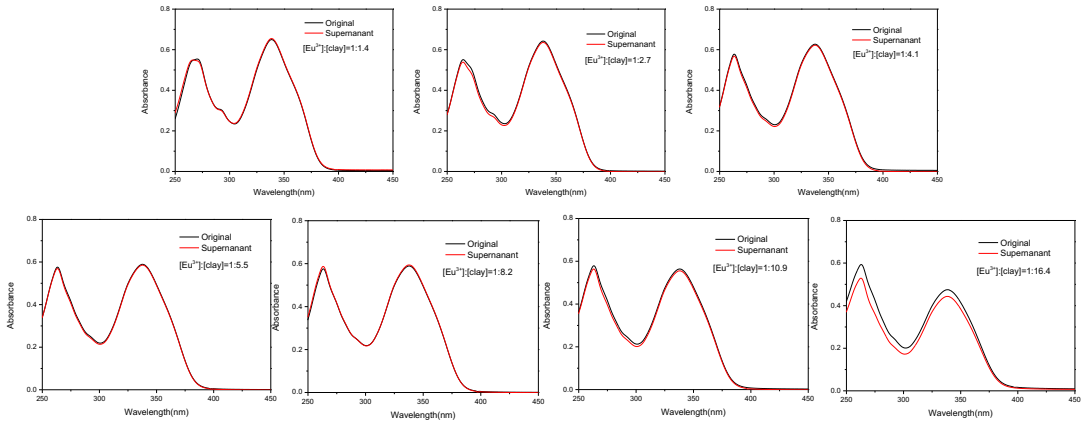

Figure 2-6 Absorption spectra of $Eu(tta)_3phen$/smectite hybrid solutions and their supernatants with different smectite content.

Table 1. Emission lifetime (τ) and contribution (%) of τ_1 and τ_2 components of $Eu(tta)_3phen$ and the $Eu(tta)_3phen$/smectite hybrid solutions

	Hybrid solution		**Supernatant**	
[Eu^{3+}]:[clay]	τ_1 (ms)	τ_2(ms)	τ_1 (ms)	τ_2 (ms)
1:0	0.65	-	0.65	-
1:1.4	0.63	-	0.63	-
1:2.7	0.62	-	0.62	-
1:4.1	0.62	-	0.62	-
1:5.5	0.62	-	0.62	-
1:8.2	0.62	-	0.62	-
1:10.9	0.62 (95.95%)	1.6 (4.05%)	0.63	-
1:16.4	0.62 (90.72%)	1.5 (9.28%)	0.62 (96.46%)	1.9 (3.54%)

We measured luminescence lifetime of the supernatant solutions (**Figure 2-5(b)**). The result showed that the decay curves of the [Eu^{3+}]:[clay] = 1:10.9 and 1:16.4 become

almost a single lifetime component of 0.62 ms which is the same as shorter lifetime of the original solution. And also, the longer lifetime components over 1 ms are almost eliminated by centrifugation treatment. This also indicated that the longer luminescent components were attributed to the Eu(III) complexes adsorbed on the smectite, and that the Eu(III) complexes was removed with smectite by centrifuge treatment. Therefore, two luminescent components of $Eu(tta)_3phen$ are present in a hybrid solution: when smectite content is low, only short luminescent component is present. This shorter lifetime component would be attributed to $Eu(tta)_3phen$ complex having relatively weaker interaction with smectite. When smectite amount became larger, longer luminescent component (τ_2) of the $Eu(tta)_3phen$ appears because $Eu(tta)_3phen$ is strongly adsorbed on the smectite.

2.1.3 Judd−Ofelt analysis of $Eu(tta)_3phen$/smectite hybrid materials

To thoroughly analyze the coordination environment of Eu(III) complexes based on emission spectra, photophysical parameters were theoretically estimated using the Judd−Ofelt theory via LUMPAC software[138]. The interaction of the ligand field is represented by the Judd−Ofelt parameter Ω_λ (λ = 2, 4, and 6). The Ω_2 parameter ($^5D_0 \rightarrow {}^7F_2$) is associated with the hypersensibility around the Eu^{3+} and is influenced by the covalency of the ligand field and the symmetry surrounding the emitter ion. Higher Ω_2 values indicate a more covalent and asymmetric chemical environment. The Ω_4 parameter ($^5D_0 \rightarrow {}^7F_4$) reflects ion–ligand and ion–ion bond distances, with larger Ω_4 values corresponding to shorter bond lengths[139]. The $^5D_0 \rightarrow {}^7F_6$ transition was not observed experimentally. Therefore, the experimental Ω6 parameters could not be determined. The calculated values of Ω_2 and Ω_4 for the $Eu(tta)_3phen$/smectite hybrid materials are listed in **Table 2**. As the smectite content increases, Ω_2 first increases and then decreases. For $[Eu^{3+}]$:[clay] =1:4.1, large Ω_2 value is attributed to the influence of smectite on the coordinative environment of Eu^{3+} ions, improving the luminescence intensity of the $Eu(tta)_3phen$ complexes in the presence of smectite. The Ω_4 values of the $Eu(tta)_3phen$/smectite hybrid materials are slightly higher than those of the pure complex, indicating a short bond distance between the Eu^{3+} ion and ligand in the hybrid solutions. This indicates that the interaction between $Eu(tta)_3phen$ and smectite affects the bond distances. This result is consistent with the structural distortion and perturbed ligand field of $Eu(tta)_3phen$, as discussed previously from the results of the absorption and photoluminescent spectral analyses.

The luminescent quantum efficiency (Φ_{Ln}) of the $^5D_0 \rightarrow {}^7F_{0\text{-}4}$ transitions in Eu^{3+} is a key factor in determining the luminescent properties of the complex, and Φ_{Ln} is defined

as $k_r/(k_r + k_{nr})$, where k_r represents the total radiative transition rate of the $^5D_0 \rightarrow {}^7F_{0\text{-}4}$ transitions, and k_{nr} denotes the nonradiative transition rate. As presented in **Table 2**, as the smectite content increases, the Eu(tta)$_3$phen complex interacts with smectite, leading to an increase in the k_r value, a decrease in the knr value, and an increase in the Φ_{Ln} value of Eu^{3+}. When [Eu^{3+}]:[clay] =1:4.1, k_r increases from 779 to 889 s^{-1}, implying that the probability of light emission from the excited state increases with the addition of smectite. This result is consistent with the low symmetry structure around the Eu^{3+} ion discussed previously. Decrease of k_{nr} (from 759 to 720 s^{-1}) also indicates that smectite suppresses the vibrational or rotation of Eu(III) complex in the smectite hybrid solution. In fact, suppression of the non-radiative deactivation process has been widely observed in various luminescent molecules incorporated into clay nanosheets[140]. The decrease in k_{nr} and the corresponding increase in k_r enhance the emission quantum efficiency of the Eu(III) complexes. This result is consistent with the low symmetry structure around the Eu^{3+} ion discussed previously.

Table 2. Judd–Ofelt parameters for the $^5D_0$ luminescence of the Eu(tta)$_3$phen complex and Eu(tta)$_3$phen/smectite hybrid solutions

[Eu^{3+}]:[clay]	Ω_2/ (10^{-20} cm^2)	Ω_4/ (10^{-20} cm^2)	k_r (s^{-1})	k_{nr} (s^{-1})	Φ_{Ln} (%)
1:0	22.6	1.7	779	759	50.7
1:1.4	23.7	1.8	812	754	51.8
1:2.7	24.6	1.7	839	751	52.8
1:4.1	26.2	1.8	889	720	55.3
1:5.5	25.5	1.7	868	731	54.3
1:8.2	24.7	1.8	844	738	53.3
1:10.9	23.5	1.8	808	702	53.5
1:16.4	20.2	1.7	703	745	48.6

When [Eu^{3+}]:[clay] =1:5.5–1:8.2, the interaction between Eu(tta)$_3$phen and smectite reaches saturation, as indicated by the stable absorption wavelength and absorbance. A single exponential fluorescence lifetime indicates that no new interactions occur between Eu(tta)$_3$phen and smectite. The excess of smectite alters the microenvironment surrounding the Eu^{3+} ions, increasing symmetry and resulting in a decrease in k_r and an increase in k_{nr}. Consequently, Φ_{Ln} decreases, leading to a decrease in luminescence intensity. When [Eu^{3+}]:[clay] = 1:10.9–1:16.4, a small part of Eu(tta)$_3$phen adsorbed on

smectite strongly, resulting in luminescence quenching[141]. On the other hand, the presence of a considerable amount of smectite renders the solution turbid, causing light scattering, which diffuses both the excited and emitted lights, reducing the amount of effective detection of the Eu(III) complex luminescence. Compared with $[Eu^{3+}]$:[clay] = 1:0, this explains why Φ_{Ln} decreases by only 2%, but the luminescence intensity decreases by 54% when $[Eu^{3+}]$:[clay] = 1:16.4.

2.2 Effect of smectite on the photoluminescence of Eu(tta)$_3$phen in film state

The fabrication of luminescent films is important for the application of luminescent materials in optical devices. In this study, the primary objective of using PMMA was to prepare more uniform films, thereby enhancing the accuracy of the measurement results. With the addition of 5 wt% PMMA, the luminescence intensity showed no significant change compared with the pure Eu(tta)$_3$phen (**Figure 2-7**). 5wt% PMMA was added to the Eu(tta)$_3$phen/smectite hybrid solutions ($[Eu^{3+}]$:[clay] from 1:0 to 1:16.4) to prepare luminescent films with unique transparency.

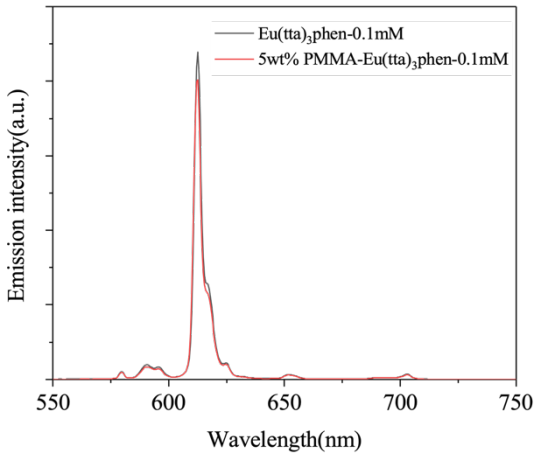

Figure 2-7 Emission spectra of Eu(tta)$_3$phen and Eu(tta)$_3$phen/PMMA hybrid solution. Excitation wavelength is 340 nm.

Follow this, under UV-light illumination, red emission can be observed (**Figure 2-8(b) and Figure 2-9(b)**). First, the films were prepared using a dip-coating method (**Figure 2-8**). The film thickness of the samples shown in **Figure 2-8** remains consistent, approximately 0.03 ± 0.005 μm. Compared with the case of the PMMA/Eu(tta)$_3$phen mix solution (1:0), the change in luminescence intensity shown in **Figure 2-8(c)** indicates that smectite can improve the luminescence intensity of Eu(tta)$_3$phen in the

film state. The trend of the luminescence intensity of the $Eu(tta)_3phen$ in the film state containing smectite content aligns consistently with that of $Eu(tta)_3phen$ in the solution state.

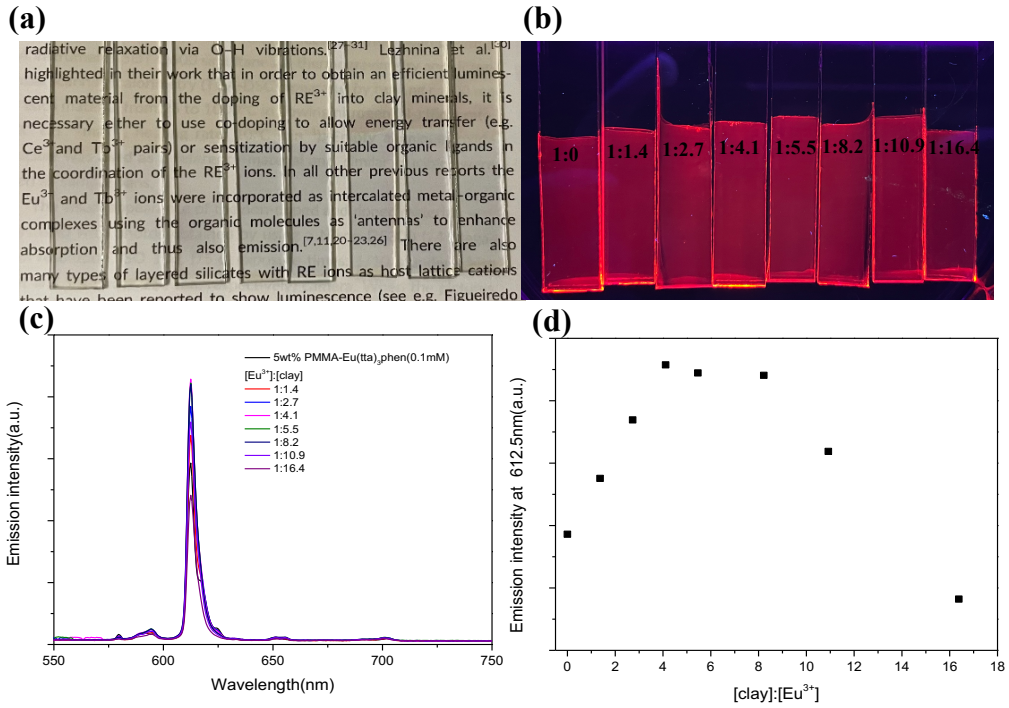

Figure 2-8 Luminescent and transparent films were prepared through dip-coating method by using $Eu(tta)_3phen$/smectite/PMMA solutions on glass substrate. Photographs of the same (a) under daylight and (b) UV-light irradiation; (c) Emission spectrum excited at 340 nm of the thin film, (d) Emission intensity at 612.5nm with the ratio of [clay]:[Eu^{3+}] from 0:1 to 16.4. The film samples in (a) and (b) are in the same order([Eu^{3+}]:[clay] from 1:0 to 1:6.4).

In addition, as shown in **Figure 2-9**, the films are prepared using a drop-coating method. When [Eu^{3+}]:[clay] is lower than 1:4.1, the non-uniform luminescence distributions are observed on the film surface under UV-light illumination (**Figure 2-9 (b)**) ([Eu^{3+}]:[clay] =1:0–1:2.7). Besides, the surface profile (**Figure 2-10**) shows that the surface of the film is non-uniform, and the edges are thicker than the middle. However, as the smectite content increases, the surfaces of the films become smoother and exhibit homogenous red emission from whole surface. This demonstrates the significance of smectite content in the fabrication of uniform films. Therefore, smectite enhances the luminescence intensity and surface smoothness of the Eu(III) complex in the film state. The excellent solution processing properties of the hybrid system demonstrate great potential for applications in various fields, such as optoelectronics and imaging.

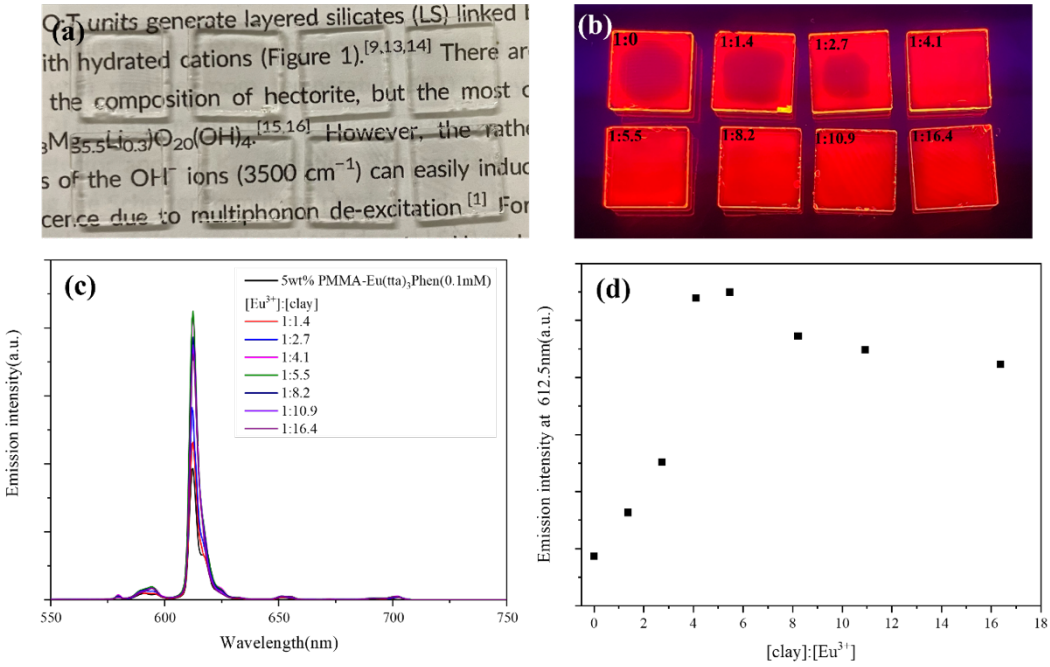

Figure 2-9 Luminescent and transparent films prepared using the drop-coating method by dropping Eu(tta)$_3$phen/smectite/PMMA solutions into a glass substrate. Photographs of the same (a) under daylight and (b) ultraviolet-light irradiation; (c) emission spectrum of the thin film excited at 340 nm and (d) emission intensity at 612.5 nm with the ratio of [clay]:[Eu^{3+}] from 0:1 to 16.4:1. Film samples in (a) and (b) are in the same order ([Eu^{3+}]:[clay] from 1:0 to 1:16.4).

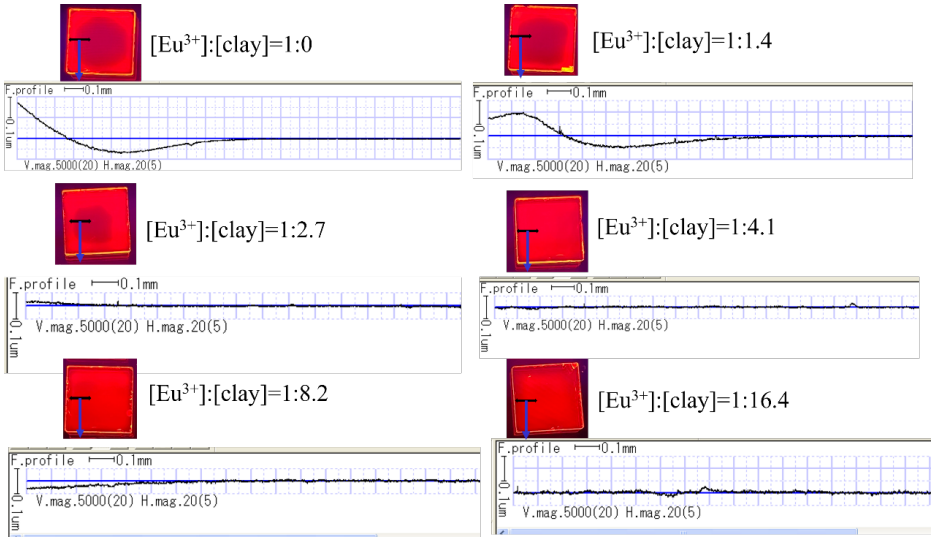

Figure 2-10 Six film samples were selected for surface profile analysis. Each sample image includes a photograph taken under UV-light illumination (top), and the surface profile of the films (down), measured using a step meter. The measured length for the surface profile is 4 mm.

2.3 Summary

In the review of Chapter 1, Most studies utilize the ion-exchange method to incorporate Eu^{3+} ions into clay layers, followed by the addition of ligands to synthesize Eu(III) complex-clay-based hybrid materials. However, the hybrid materials prepared by this method exhibit some disadvantages such as low transparency. In this research, we use smectite with functional groups (methyltri-n-octylammonium ions), allowing for better dispersion in polar solvents. The photophysical properties of Eu(III) complex-smectite hybrid material was studied.

Chapter 2 investigates the effect of different smectite contents on the photophysical properties of $Eu(tta)_3phen$ complexes. Using a simple doping method, a highly luminescent $Eu(tta)_3phen$-smectite hybrid solutio was prepared. The comprehensive photophysical properties of the $Eu(tta)_3phen$/smectite hybrid dispersion were systematically studied using UV-Vis absorption spectroscopy, emission spectroscopy, luminescence lifetime measurements, and Judd-Ofelt analysis. The photophysical analysis indicated that the interaction between $Eu(tta)_3phen$ and smectite caused structural distortion of $Eu(tta)_3phen$, thereby enhancing the probability of electric dipole transitions. Judd-Ofelt parameters revealed that, at a $[Eu^{3+}]$:[clay] ratio of 1:4.1, the I_{rel} and Ω_2 values indicated that the Eu^{3+} ions exhibit the lowest symmetry due to their interaction with smectite. Moreover, the increase in the radiative rate (k_r) and the decrease in the non-radiative rate (k_{nr}) suggest that the interaction between $Eu(tta)_3phen$ and smectite suppresses molecular vibrations, leading to enhanced luminescence intensity and quantum efficiency.

Additionally, highly luminescent and transparent $Eu(tta)_3phen$/smectite/PMMA films were prepared using simple dip-coating and drop-casting methods. Smectite enhanced both the luminescence intensity and surface smoothness of the films. These luminescent hybrid materials, which exhibit excellent processability in organic solutions, hold significant potential for applications in optoelectronics and imaging technologies.

Chapter 3

Eletrochemical modulation of emission and coloration by using luminescence Eu(III) complex and electrochromic material (HV^{2+}) hybridized with smectite

Chapter 3 Eletrochemical modulation of emission and coloration by using luminescence Eu(III) complex and electrochromic material (HV^{2+}) hybridized with smectite

Chapter 2 explores the photophysical properties of Eu(III) complexes hybridized with smectite. The resulting Eu(III) complex/smectite hybrid material exhibits strong luminescence intensity and excellent film-forming ability, with smectite playing a key role in enhancing the photophysical performance of the Eu(III) complex. Additionally, we are interested in investigating the unique electrochemical characteristics of this hybrid material. Therefore, Chapter 3 will focus on the electrofluorochromic (EFC) properties of the Eu(III) complex-smectite hybrid system in conjunction with an electrochemically active material.

Chapter 1 presents pioneering research on the integration of electrochromic (EC) materials, specifically viologen derivatives (HV^{2+}), with electrofluorochromic (EFC) materials, such as Eu(III) complexes, for the fabrication of dual-mode display (DMD) devices. Layered clay compounds, known for their exceptional stability and high ion exchange capacity, serve as ideal platforms for incorporating these functional materials. Although clay itself has low conductivity, it can still exhibit electrochemical activity when combined with electrochemically active materials. As a result, incorporating electrochemically active materials into clay for use as electrode materials has emerged as a key research focus. Meanwhile, clay-based luminescent hybrid materials have attracted considerable attention, as they not only preserve the superior luminescent properties of lanthanide complexes but also improve their stability. However, the development of multifunctional EFC materials and devices utilizing clay compounds remains limited, particularly in the investigation of EC/EFC multifunctional materials and their applications.

As discussed in the Chapter 1, the application of electroluminescent chromic materials in luminescent imaging display devices is hindered when these materials are in solution form. To effectively utilize them for sensors, security applications, and imaging displays, it is crucial to coat and pattern functional electrodes to achieve desired features, including rapid luminescent response, substantial on/off contrast, and cycling stability. Recent research has concentrated on the immobilization of functional components onto electrodes by applying polymer-based electroluminescent chromic materials[142, 143] or dye-anchored inorganic layers[122, 144]. This immobilization approach not only enhances luminescent switching contrast but also allows radicals

generated by the electric field to reside close to the luminescent region, facilitating efficient luminescence quenching through energy transfer mechanisms.

This chapter details the fabrication of a novel electrochemical DMD device utilizing smectite clay compounds, where Eu(III) complexes serve as luminescent molecules and heptyl viologen (HV^{2+}) functions as the electrochromic component, both embedded within the smectite matrix (chemical structures shown in **Figure 3-1**). A smectite/ HV^{2+}/Eu(III) complex film-modified working electrode was fabricated, and the photophysical and electrochemical properties of this multifunctional hybrid material were thoroughly investigated. The study successfully demonstrated the electrochemical modulation of both coloration and luminescence.

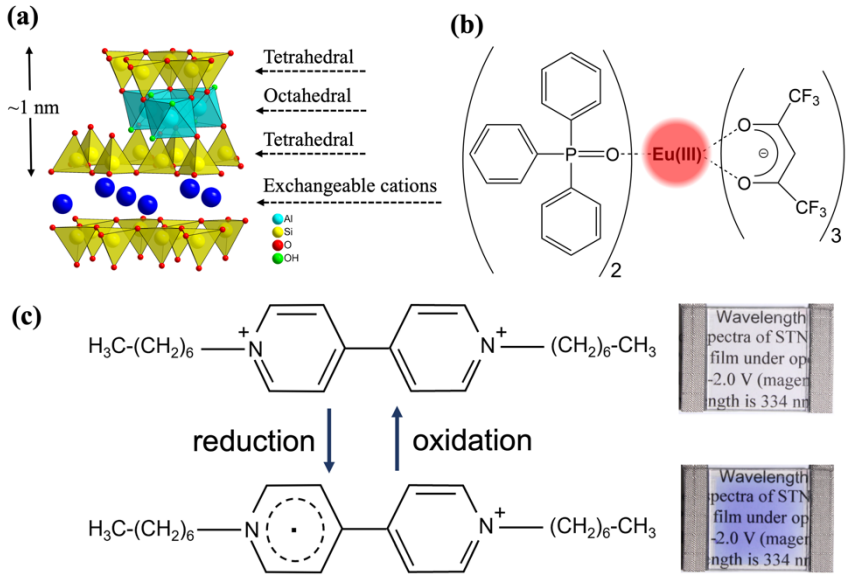

Figure 3-1 Chemical structure of (a) Smectite, (b) $Eu(hfa)_3(TPPO)_2$, and (c) HV^{2+}.

Preparation of the hybrid solutions

STN solutions were prepared by dispersing 1 wt.% STN in acetonitrile. For the STN/HV^{2+} hybrid solution, 1 wt.% STN and 1.2 mmol/L HV^{2+} were dispersed and dissolved in acetonitrile in case 50% vs CEC ratio. Similarly, the STN/$Eu(hfa)_3(TPPO)_2$ hybrid solution was prepared by dispersing 1 wt.% STN and 0.8 mmol/L $Eu(hfa)_3(TPPO)_2$ in acetonitrile in case 50% vs CEC ratio. The STN/HV^{2+}/ $Eu(hfa)_3(TPPO)_2$ hybrid solution (1 wt.%, 1.2 mmol/L, and 0.8 mmol/L, respectively) was prepared in acetonitrile for a 50%:50% vs CEC ratio. Additionally, a supporting electrolyte solution was prepared by dissolving 200 mmol/L TBAP in PC solvent. All solutions were prepared at room temperature.

Preparation of 3-electrodes cell

The ITO electrode surface was first cleaned and subjected to UV/O_3 treatment for 20 minutes. Following this, 0.2 ml of the STN/HV^{2+} solution, STN/$Eu(hfa)_3(TPPO)_2$ solution, and STN/HV^{2+}/$Eu(hfa)_3(TPPO)_2$ dispersion solutions were drop-cast onto the ITO electrodes. After drying at room temperature, the resulting films served as working electrodes (active area: 2 cm^2). A Pt wire functioned as the counter electrode, while an Ag/Ag^+ electrode was used as the reference, both immersed in the electrolyte solution.

Preparation of 2-electrode device

The ITO electrode surface was first cleaned and subjected to UV/O_3 treatment for 20 minutes. Following this, 0.2 ml of the STN/HV^{2+} solution, STN/$Eu(hfa)_3(TPPO)_2$ solution and STN/HV^{2+}/$Eu(hfa)_3(TPPO)_2$ solutions were drop-cast onto the center of the plastic spacer on the ITO electrode surface. After drying at room temperature, the corresponding films were formed. The 2-electrode device was prepared by sandwiching the electrolyte solution between an ITO electrode modified with the STN/HV^{2+}, STN/$Eu(hfa)_3(TPPO)_2$, or STN/HV^{2+}/$Eu(hfa)_3(TPPO)_2$ film and an unmodified ITO electrode.

3.1 The interaction between Eu(III) complex and HV^{2+} in the presence of smectite

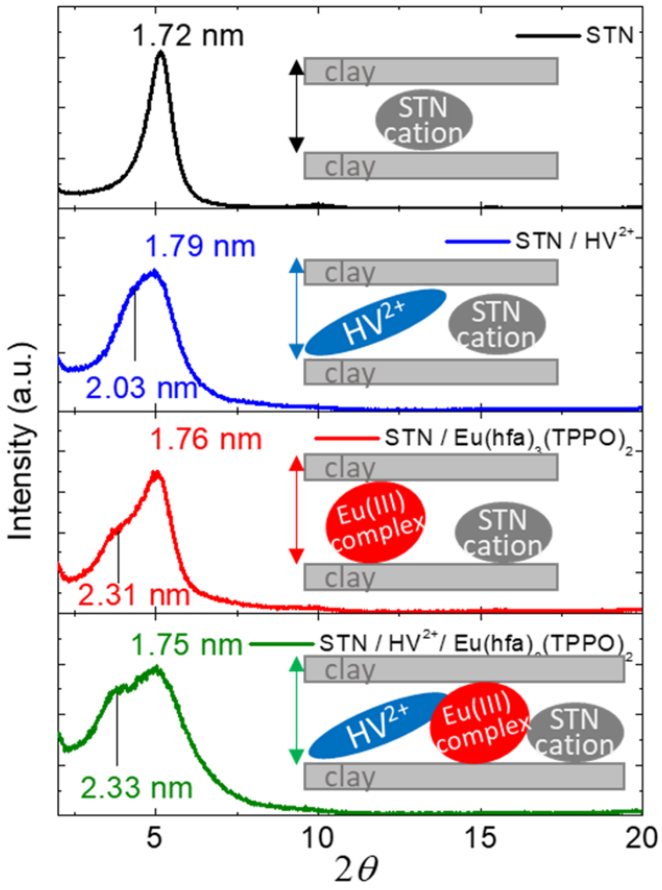

Figure 3-2 X-ray Diffraction (XRD) spectra of STN film, STN/ HV^{2+} film, STN/ $Eu(hfa)_3(TPPO)_2$ film, STN/ HV^{2+}/ $Eu(hfa)_3(TPPO)_2$ film

In this study, the intercalation of $Eu(hfa)_3(TPPO)_2$ and HV^{2+} into the STN layers was analyzed using XRD (**Figure 3-2**). The pristine smectite, containing metal ions or H_2O molecule, exhibits the 001 peak at approximately 6.5 degree[145]. Upon intercalation of methyltri-n-octylammonium ions, the interlayer spacing increases, shifting the 001 peak to 5°[146]. Using the Bragg equation ($2d\sin\theta = n\lambda$), the interlayer spacing *d* of pristine STN was determined to be around 1.72 nm. Compared to the STN film, the STN/ HV^{2+} film displayed a broader peak at 5° with an additional shoulder peak at 4.35°, expanding the interlayer spacing to 2.03 nm. The spacing for HV^{2+} molecules varied between 0.43 nm and 2.6 nm, depending on their insertion orientation (**Figure 3-3(a)**), while the STN layer itself had a thickness of approximately 1 nm[147]. These findings suggest that HV^{2+} molecules intercalate into the STN layer at a specific angle.

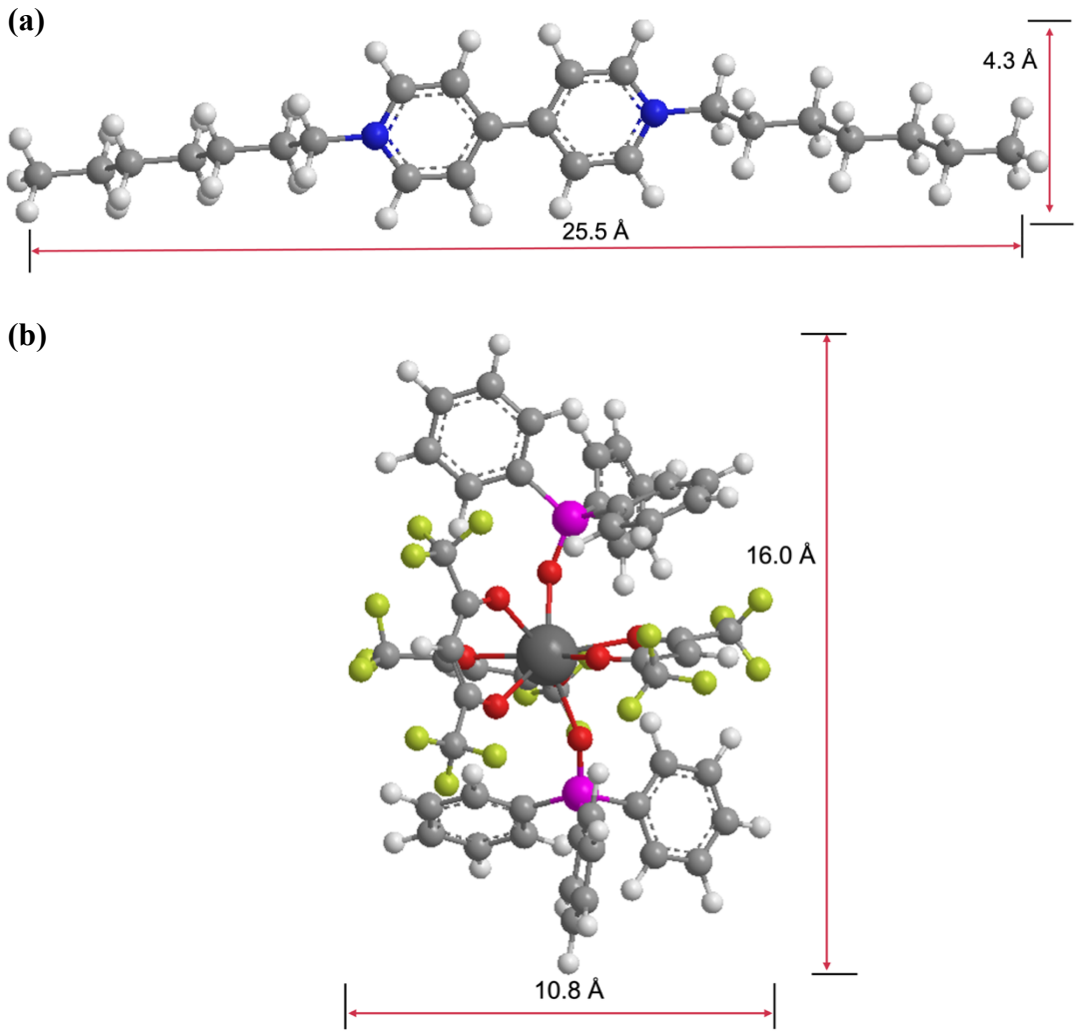

Figure 3-3 (a) Chemical structure diagram of HV^{2+} molecules obtained using MM3 calculation in Chem 3D application. Interatomic distances of the HV^{2+} molecules ranging from approximately 0.43 nm to 2.55 nm. (b) Molecular structure diagram of $Eu(hfa)_3(TPPO)_2$ complex drawn using single crystal X-ray measurement data from ref [148]. Interatomic distances of the $Eu(hfa)_3(TPPO)_2$ complex ranging from approximately 1.08 nm to 1.6 nm.

Similarly, for the STN/ $Eu(hfa)_3(TPPO)_2$ film, the shoulder peak shifted to approximately 3.8°, corresponding to an increase in interlayer spacing to 2.31 nm. The $Eu(hfa)_3(TPPO)_2$ molecule exhibits a size range from a minimum of 1.08 nm to a maximum of 1.6 nm (**Figure 3-3 (b)**), confirming its insertion into the STN interlayers. The STN/ HV^{2+}/ $Eu(hfa)_3(TPPO)_2$ film exhibited both HV^{2+} and $Eu(hfa)_3(TPPO)_2$, as indicated by the broad peak at 5° and the shoulder peak around 3.8°, demonstrating the successful intercalation of both components within the STN layers.

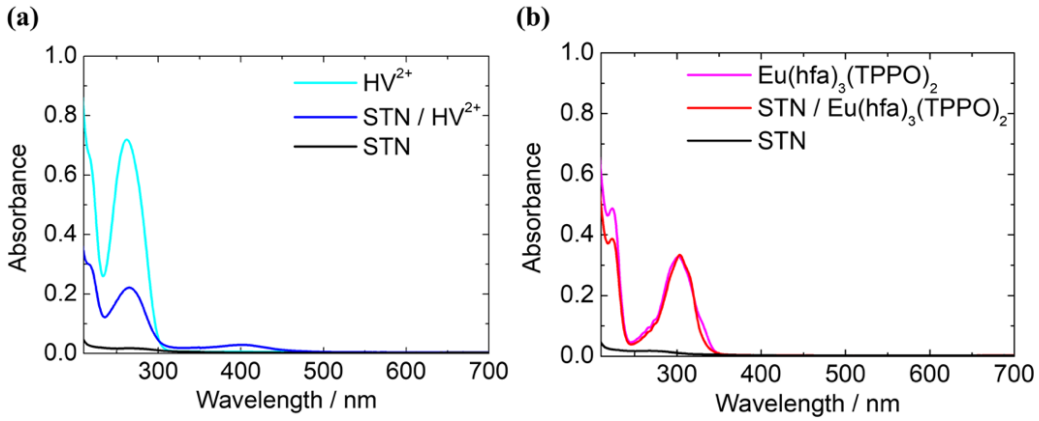

Figure 3-4 (a) Absorption spectra of the HV^{2+} solution, STN/HV^{2+} solution, and clay solution; (b) Absorption spectra of $Eu(hfa)_3(TPPO)_2$ solution, STN/$Eu(hfa)_3(TPPO)_2$ solution, and clay solution.

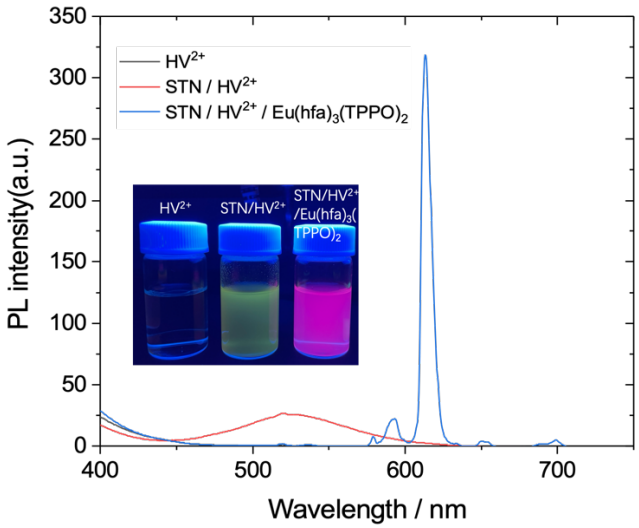

Figure 3-5 Emission spectra of HV^{2+}, STN/HV^{2+} and STN/HV^{2+}/$Eu(hfa)_3(TPPO)_2$ solutions with excitation wavelength of 260 nm. Inset: photographs of the solutions under UV irradiation.

The absorption spectra of the hybrid solutions were tested between 200 - 700 nm. As depicted in **Figure 3-4 (a)**, the HV^{2+} molecule exhibited an absorption peak around 260 nm. Notably, upon the addition of STN (blue line in **Figure 3-4(a)** and **Figure 3-6**), a new absorption peak emerged near 400 nm (inset of **Figure 3-6**). As shown in **Figure 3-5**, the emission spectra of HV^{2+}, STN/HV^{2+}, and STN/HV^{2+}/$Eu(hfa)_3(TPPO)_2$ were recorded with an excitation wavelength of 260 nm. Among these, only the STN/ HV^{2+} solution displayed an emission peak at approximately 520 nm. Under UV irradiation, the STN/HV^{2+} solution emitted green fluorescence. We speculate that the newly

observed absorption peak at 400 nm is associated with the emission peak at 520 nm. When HV^{2+} molecules are intercalated into the STN interlayer, interactions such as fixation, aggregation, or charge transfer occur between STN and HV^{2+} within the confined interlayer space. These interactions contribute to the appearance of the 400 nm absorption peak and the observed green fluorescence. Subsequently, the absorption properties of $Eu(hfa)_3(TPPO)_2$ were examined. As illustrated in **Figure 3-4(b)**, $Eu(hfa)_3(TPPO)_2$ exhibited an absorption peak at approximately 300 nm, which remained unchanged upon the addition of STN. This indicates that smectite has no impact on the absorption characteristics of $Eu(hfa)_3(TPPO)_2$.

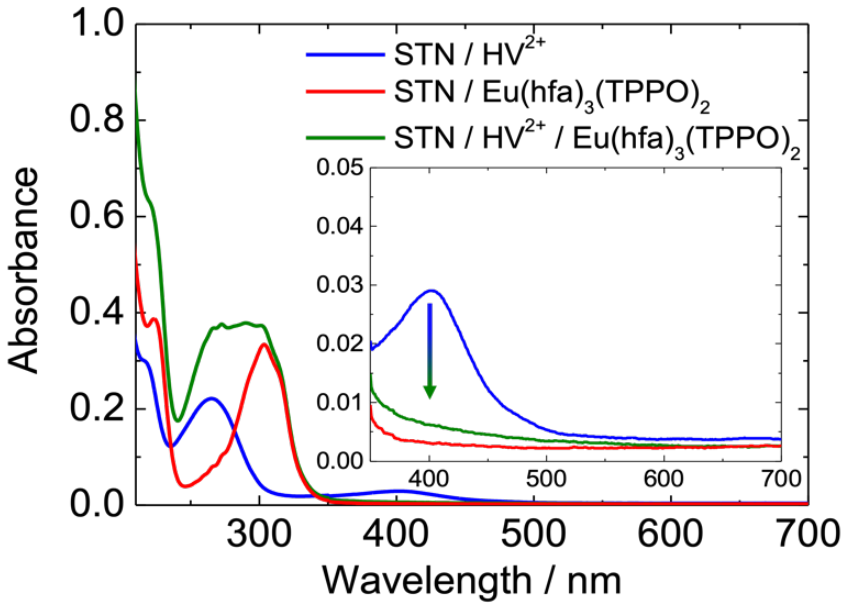

Figure 3-6 Absorption spectra of STN/ HV^{2+} solution, STN/ $Eu(hfa)_3(TPPO)_2$ solution, STN/ HV^{2+}/ $Eu(hfa)_3(TPPO)_2$ solution. Inset: enlarged view of the absorption spectrum in the range of 350 nm to 700 nm.

The absorption properties of the hybrid solutions were further analyzed. As shown in **Figure 3-6**, the STN/ HV^{2+}/ $Eu(hfa)_3(TPPO)_2$ solution exhibited a broadened peak near 290 nm, resulting from the overlapping absorption bands of HV^{2+} (around 260 nm) and the $Eu(hfa)_3(TPPO)_2$ (around 300 nm) in smectite solution. However, upon the addition of $Eu(hfa)_3(TPPO)_2$, the absorption peak around 400 nm associated with HV^{2+} molecules and the green fluorescence of the hybrid solution disappeared (**Figure 3-5**). The intercalation of $Eu(hfa)_3(TPPO)_2$ into the STN layers led to an increase in interlayer spacing, weakening or eliminating the interactions responsible for these spectral

features. This observation aligns with the XRD results presented in **Figure 3-2**. Overall, these findings confirm the coexistence of HV^{2+} and $Eu(hfa)_3(TPPO)_2$ within the STN layers.

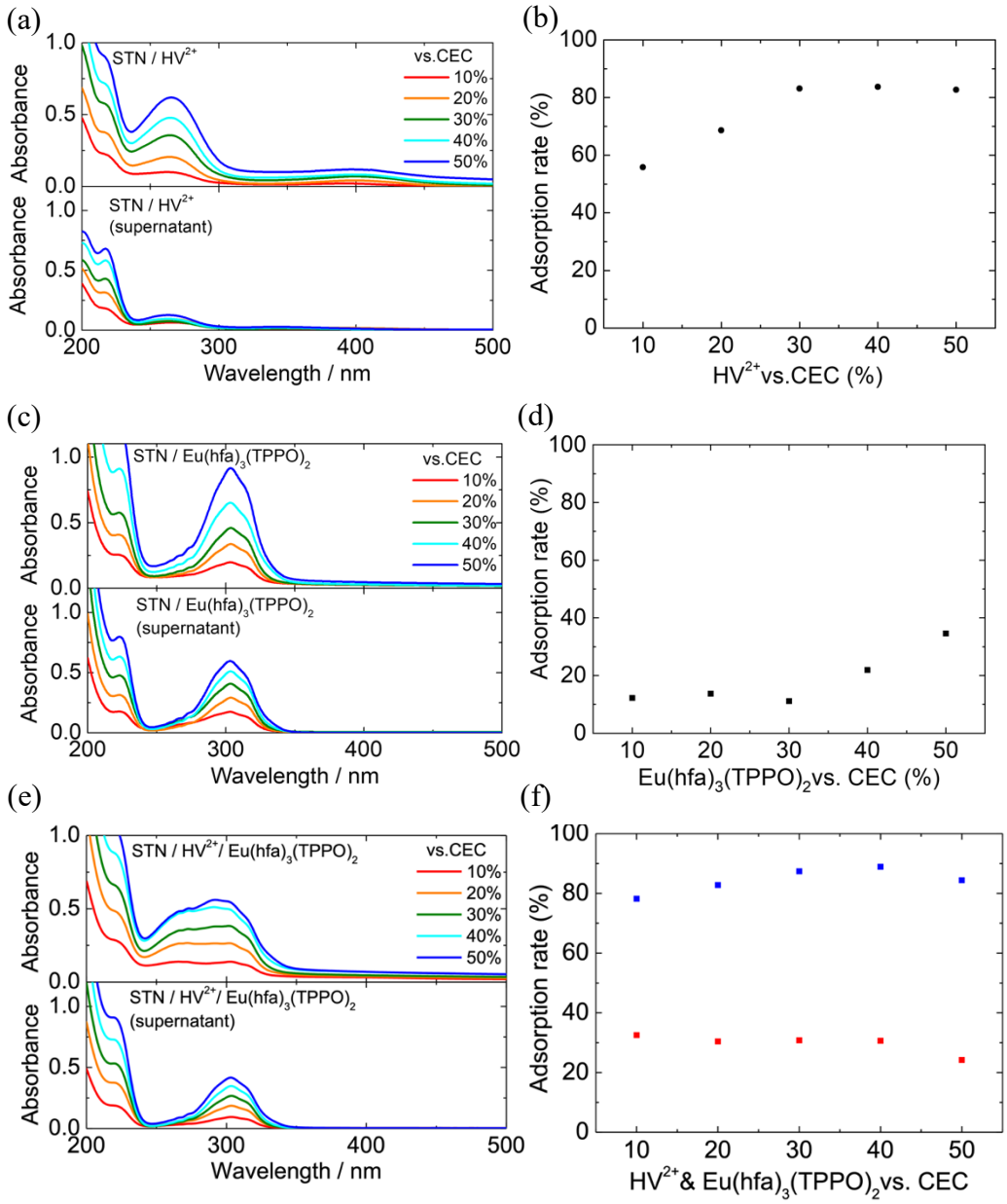

Figure 3-7 (a) Absorption spectra of the STN/HV^{2+} original hybrid solutions (top) and supernatants (bottom); (b) the adsorption rate of HV^{2+} molecule. (c) Absorption spectra of the STN/$Eu(hfa)_3(TPPO)_2$ original hybrid solutions (top) and supernatants (bottom); (d) the adsorption rate of $Eu(hfa)_3(TPPO)_2$ complex. (e) Absorption spectra of STN/ HV^{2+}/ $Eu(hfa)_3(TPPO)_2$ original hybrid solutions (top) and supernatants (bottom); (f) Adsorption ratios of HV^{2+} (blue dots) and $Eu(hfa)_3(TPPO)_2$ (red dots) at different ratios.

To assess the adsorption capacity of HV^{2+} and $Eu(hfa)_3(TPPO)_2$ onto STN, the absorption spectra of the STN/HV^{2+}/$Eu(hfa)_3(TPPO)_2$ hybrid solutions and their supernatants after centrifugation were analyzed. As shown in **Figure 3-7(a–d),** a notable reduction in absorbance was observed in the supernatant solutions following centrifugation for both STN/HV^{2+} and STN/$Eu(hfa)_3(TPPO)_2$ solutions. This decrease indicates that HV^{2+} and $Eu(hfa)_3(TPPO)_2$ were effectively intercalated into the STN layers and subsequently removed during centrifugation. Based on absorbance measurements, the adsorption efficiencies of HV^{2+} and $Eu(hfa)_3(TPPO)_2$ were estimated to be approximately 80% and 35%, respectively. **Figure 3-7 (e-f)** illustrates a significant reduction in the absorption peak of HV^{2+} near 270 nm after centrifugation, whereas the absorption peak of $Eu(hfa)_3(TPPO)_2$ near 300 nm shows a comparatively smaller decrease. This suggests that HV^{2+} is more readily adsorbed by the STN matrix due to the negative charges of the STN layers, which preferentially attract cationic species such as HV^{2+}. In contrast, $Eu(hfa)_3(TPPO)_2$ interacts with STN primarily through hydrophobic interactions with methyltri-n-octylammonium ions, which possess long hydrophobic alkyl chains. Although van der Waals forces are relatively weak, they contribute to intermolecular interactions and play a supportive role in the adsorption process. Furthermore, our previous studies have examined the interactions between non-ionic Eu(III) complexes and alkyl ammonium cations in solution, solid-state, and polymer matrices such as DNA-CTMA[80, 149]. Compared to the STN/$Eu(hfa)_3(TPPO)_2$ solution without HV^{2+} (Figure 3-7(c–d)), the adsorption efficiency of $Eu(hfa)_3(TPPO)_2$ in the STN/HV^{2+}/$Eu(hfa)_3(TPPO)_2$ hybrid solution was higher under lower CEC conditions. This enhancement is attributed to HV^{2+} expanding the STN interlayer spacing, thereby promoting the adsorption of the Eu(III) complex. As shown in **Figure 3-7(f)**, the estimated adsorption ratios indicate that approximately 80% of HV^{2+} and around 20% of $Eu(hfa)_3(TPPO)_2$ are adsorbed under a 50%:50% vs CEC condition. Consequently, 50% of the anionic sites in STN were occupied by $Eu(hfa)_3(TPPO)_2$ and HV^{2+}, while the remaining 50% were retained by the original methyltri-n-octylammonium ion cations.

Additionally, as shown in **Figure 3-8**, the emission spectra and time-resolved emission decay curves of $Eu(hfa)_3(TPPO)_2$, STN/$Eu(hfa)_3(TPPO)_2$, and STN/HV^2/$Eu(hfa)_3(TPPO)_2$ solutions confirm that the Eu(III) complex remains in a stable molecular form within these hybrid solutions without dissociation[150]. This is evidenced by the unchanged number and position of the emission transitions for Eu^{3+} ($^5D_0 \rightarrow {}^7F_J$, J = 0, 1, 2, 3, 4), with the $^5D_0 \rightarrow {}^7F_0$ transition displaying a single peak, indicating a predominant and uniform chemical environment surrounding the Eu(III) ions (**Figure 3-8 (a)**)[151]. Furthermore, as depicted in **Figure 3-8(b)**, all solutions

exhibit emission decay curves characterized by a single exponential component (~0.84 ms). This mono-exponential decay behavior suggests the presence of a single emitting species of the Eu(III) complex[152].

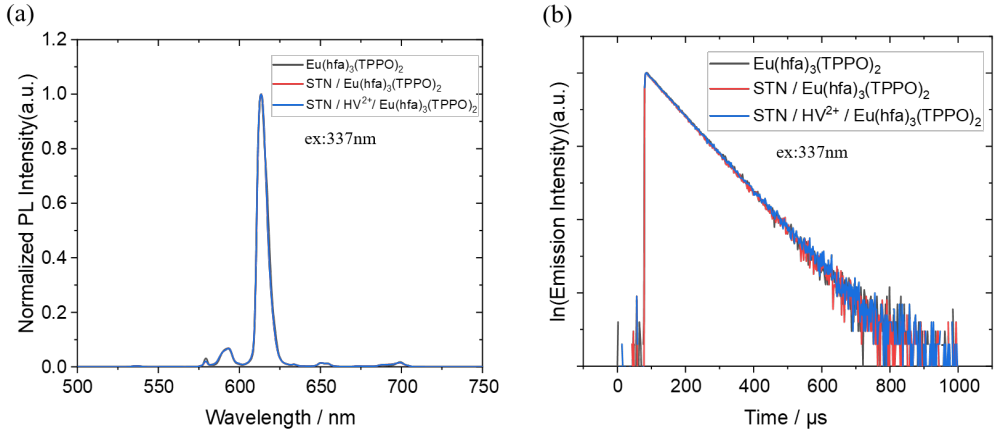

Figure 3-8 (a) Normalized emission spectra of $Eu(hfa)_3(TPPO)_2$, $STN/Eu(hfa)_3(TPPO)_2$ and $STN/HV^{2+}/Eu(hfa)_3(TPPO)_2$ in the solution. (b) Emission decay curves of $Eu(hfa)_3(TPPO)_2$, $STN/Eu(hfa)_3(TPPO)_2$ and $STN/HV^{2+}/Eu(hfa)_3(TPPO)_2$ in the solution at 613 nm ($^5D_0 \rightarrow {}^7F_2$). Excitation wavelength was 337 nm.

3.2 Eletrochemical properties of Eu(III) complex and HV^{2+} in the presence of smectite

In the previous section, we explored the interaction and photophysical properties of the hybrid materials in detail. HV^{2+} and Eu(III) complex were partially inserted into the interlayer of smectite. In this chapter, we will focus on the electrochemical performance of STN/HV^{2+} film, $STN/Eu(hfa)_3(TPPO)_2$ film, and $STN/HV^{2+}/Eu(hfa)_3(TPPO)_2$ film modified on ITO electrode. Cyclic voltammetry (CV) measurements and in situ absorbance changes at 610 nm were recorded (**Figure 3-9 (a)**). The $STN/Eu(hfa)_3(TPPO)_2$-based electrode does not exhibit any significant reduction or oxidation reactions within the investigated potential range. In contrast, the reductive current of the STN/HV^{2+} film-modified electrode increased at 610 nm during the negative potential sweep, which corresponds to the characteristic electrochromic (EC) reaction of HV^{2+} [153]. This suggests that despite HV^{2+} being intercalated into the STN matrix, which is inherently an insulator, redox hopping can still occur, facilitating redox reactions[154]. For the $STN/HV^{2+}/Eu(hfa)_3(TPPO)_2$ film-modified electrode, both the reduction current and absorbance near -0.7 V nearly doubled compared to the STN/HV^{2+} film-modified electrode. This enhancement is attributed to the incorporation of the $Eu(hfa)_3(TPPO)_2$, which expanded the interlayer spacing of the STN matrix, as

confirmed by the XRD results in **Figure 3-2**. The increased interlayer distance allowed more supporting electrolytes to penetrate the interlayer space, thereby improving the redox activity of HV^{2+}. **Figure 3-9** (b) presents the chronoamperometric results for the STN/HV^{2+} film and STN/HV^{2+}/$Eu(hfa)_3(TPPO)_2$ films used as the working electrodes. The insert table summarizes the reaction charge quantities and the reaction ratio of HV^{2+} molecules within the films. By integrating the current values, the reaction charge was determined to be 0.71×10^{-3} C for the STN/HV^{2+} film and 1.39×10^{-3} C for the STN/HV^{2+}/$Eu(hfa)_3(TPPO)_2$ film.

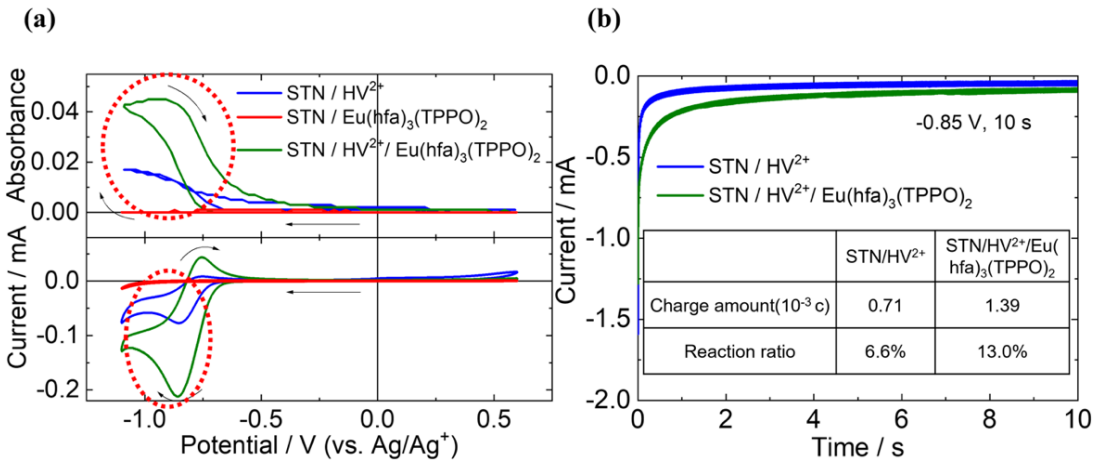

Figure 3-9 (a) Change in absorbance at 610 nm (top) and cyclic voltammograms (bottom) of STN/HV^{2+}, STN/$Eu(hfa)_3(TPPO)_2$, STN/HV^{2+}/$Eu(hfa)_3(TPPO)_2$; (b) Chronoamperometric curves of STN/HV^{2+} film (blue line) and STN/HV^{2+}/$Eu(hfa)_3(TPPO)_2$ film (green line). Inserted table shows the reaction charge amount and reaction ratio of HV^{2+} molecule in the sample.

The quantity of HV^{2+} in the film was estimated based on the concentration and volume of HV^{2+} in the hybrid solution used for film preparation (0.2 ml, 1.2 mmol/L). The total amount of HV^{2+} in the reaction area was calculated to be 1.1×10^{-7} mol. By multiplying this value by the Faraday constant (96485 C mol^{-1}), the theoretical charge required for the first reduction of all HV^{2+} molecules in the reaction area was determined to be 0.011 C. Consequently, the actual reaction ratios for each film were evaluated using **Equation 1**.

$$Reaction\ ratio = \frac{Actual\ reaction\ charge\ (C)}{0.011\ (C)} \times 100\% \qquad \text{(Equation 1)}$$

As a result, the reaction ratio of HV^{2+} increased from 6.6% to 13.0% due to the presence of the Eu(III) complex. This indicates that the incorporation of $Eu(hfa)_3(TPPO)_2$ nearly doubles the reduction reaction ratio of HV^{2+}. This enhancement is attributed to $Eu(hfa)_3(TPPO)_2$ expanding the interlayer spacing of the

STN matrix, which facilitates electron movement and thereby improves the reaction efficiency of HV^{2+}, as confirmed by CV measurements.

3.3 Electrochemical switching of emission and coloration

The two-electrode electrochemical devices were constructed to demonstrate the simultaneous modulation of both emission and coloration via the EC reaction of HV^{2+}. Initially, the EC properties of a two-electrode device utilizing an STN/HV^{2+} film, without the Eu(III) complex, as the modified electrode were investigated (**Figure 3-10**). Prior to applying a bias voltage, no absorption band was detected in the visible region (400–700 nm) (black line, **Figure 3-10**). However, after applying a bias voltage of −2.0 V for 150 s, an absorption band associated with the reduced $HV^{\bullet+}$ species emerged around 610 nm (blue line, **Figure 3-10**), leading to a distinct cyan coloration.

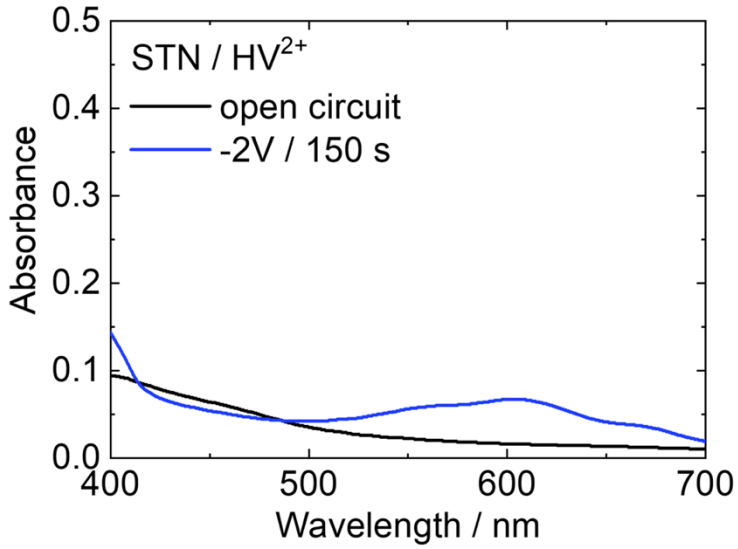

Figure 3-10 (a) Absorption spectra of the STN/HV^{2+} film under open circuit condition (black line) and applied -2.0 V for 150 s (blue line)

The optical modulation of a two-electrode EFC device containing HV^{2+} and the Eu(III) complex in clay matrix was evaluated. As shown in **Figure 3-11**, the STN/HV^{2+}/$Eu(hfa)_3(TPPO)_2$-based device exhibits no absorption between 400 nm and 700 nm when no bias voltage is applied (black line), indicating that it has a colorless and transparent appearance, which can be regarded as a "reflection-off" state (photo in **Figure 3-11 (a)**). When a bias voltage of −2.0 V was applied for 150 s, new absorption bands appeared near 400 nm and 600 nm, which can be assigned to the reduced species of HV^{+} and HV. In our previous report, the absorbance around 337 nm showed almost

no change after the reduction of the HV^{2+} molecule[128]. Therefore, the reduced species of HV^{+} and HV has a minimal impact on the absorption of the excitation light for the Eu(III) complex. As the intensity of the new absorption bands increased, the color of the device changed from colorless to cyan, representing the "reflection-on" state. Compared with the STN/HV^{2+}-based device without Eu(III) complex (**Figure 3-10**), the absorbance at 600 nm of the STN/HV^{2+}/$Eu(hfa)_3(TPPO)_2$-based device significantly increased. This is consistent with the results shown in **Figure 3-9**, wherein an increased reduction reaction ratio of HV^{2+} was observed after the addition of $Eu(hfa)_3(TPPO)_2$.

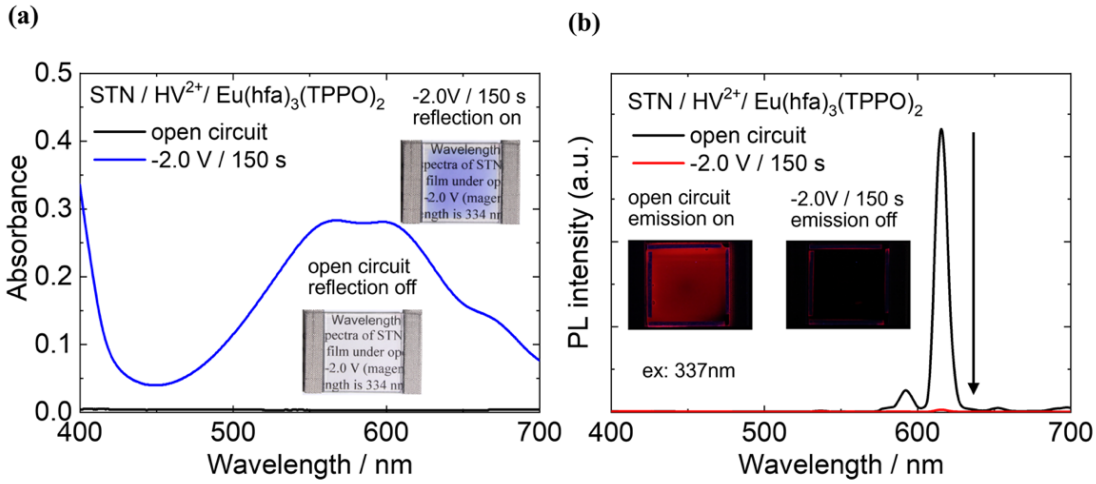

Figure 3-11 (a) Absorption spectra of STN/HV^{2+}/$Eu(hfa)_3(TPPO)_2$ film under open circuit condition (black line) and applied -2.0 V for 150 s (blue line). (b) Emission spectra of STN/HV^{2+}/$Eu(hfa)_3(TPPO)_2$ film under open circuit condition (black line) and applied -2.0 V for 150 s (red line). Excitation wavelength is 337 nm.

The photoluminescence behavior of the device during redox reactions was thoroughly examined. Under open-circuit conditions (i.e., before voltage application, black line in **Figure 3-11(b)**), $Eu(hfa)_3(TPPO)_2$ exhibited intense red emission bands upon excitation at 337 nm, corresponding to the "emission-on" state (photo in **Figure 3-11(b)**). However, upon applying a −2.0 V bias, this red emission was entirely quenched (red line), transitioning the device to an "emission-off" state, with the emission intensity decreasing by 99.3%.

Additionally, in the two-electrode device, the emission intensity and lifetime of STN/$Eu(hfa)_3(TPPO)_2$ without HV^{2+} remained unaffected by the applied bias voltage (**Figure 3-12** and **Figure 3-13(a)**). In contrast, when HV^{2+} was incorporated, the emission lifetime of the $Eu(hfa)_3(TPPO)_2$ complex in the STN/HV^{2+}/$Eu(hfa)_3(TPPO)_2$-

based device decreased upon bias application (**Figure 3-13(b)**). This strongly suggests that the colored $HV^{\bullet+}$ species played a key role in modulating the emission properties of $Eu(hfa)_3(TPPO)_2$. These results highlight that effective luminescence control can be achieved when EC materials and luminescent materials coexist within the STN matrix.

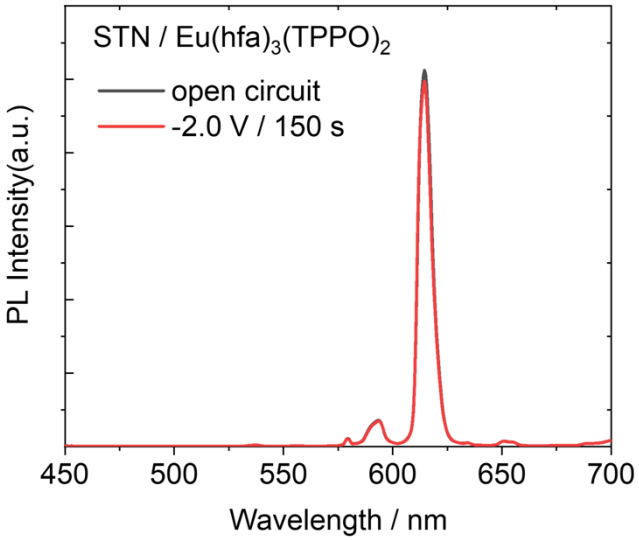

Figure 3-12 Emission spectra of STN/ $Eu(hfa)_3(TPPO)_2$ in the two electrodes device (black line: open circuit condition, red line: under bias voltage of −2 V for 150 s). Excitation wavelength was 337 nm.

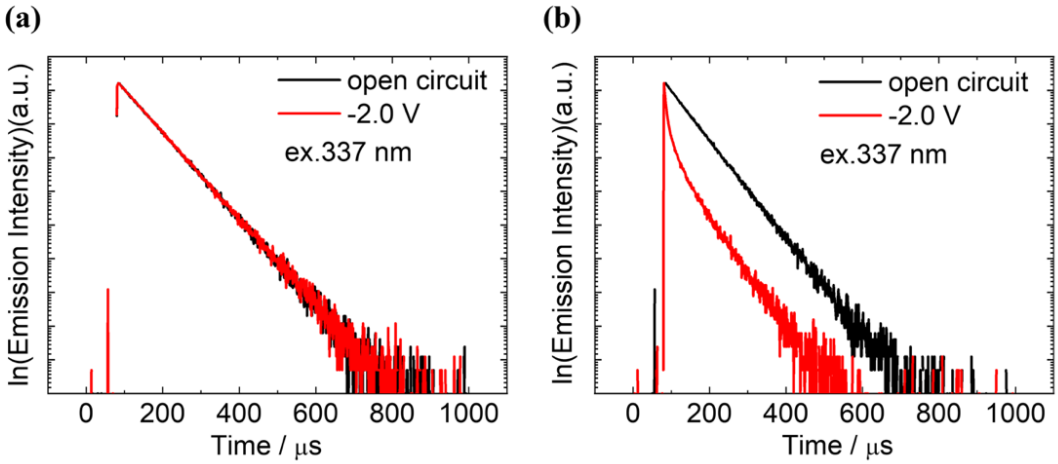

Figure 3-13 Emission decay curves at 615 nm ($^5D_0 \rightarrow {}^7F_2$) under open circuit condition (black line), and after the application of a bias voltage of −2.0 V for 150 s (red line). (a) STN/ $Eu(hfa)_3(TPPO)_2$ device and (b) STN/ HV^{2+}/ $Eu(hfa)_3(TPPO)_2$ device.

3.4 Mechanism of electrochemical modulation of emission and coloration

To explore the mechanism of luminescence modulation, the photophysical properties of the EFC device were thoroughly examined. This device featured a modified ITO electrode with STN/HV^{2+}/$Eu(hfa)_3(TPPO)_2$ as the working electrode. As depicted in **Figure 3-14**, the absorption band of the reduced $HV^{\bullet+}$ species appears around 600 nm, exhibiting significant overlap with the emission bands of $Eu(hfa)_3(TPPO)_2$. This spectral overlap facilitates efficient fluorescence resonance energy transfer (FRET) from the excited states of the Eu(III) complex to the reduced $HV^{\bullet+}$ species[155, 156]. Additionally, photoinduced electron transfer may occur from $HV^{\bullet+}$ in its reduced state to the excited $Eu(hfa)_3(TPPO)_2$, leading to the formation of a reduced $Eu(hfa)_3(TPPO)_2$ state and resulting in luminescence quenching. In our previous study, we explored similar photoinduced electron transfer processes between Eu(III) complexes and viologen derivatives. The results indicated that the absorbance of the reduced $HV^{\bullet+}$ species was unaffected by the excitation of the Eu(III) complex[157]. Furthermore, the overlap between the molecular orbitals of the inner 4f electron orbitals of Eu^{3+} ions and those of the viologen molecule was found to be minimal, which would limit the extent of electron transfer[155]. These findings suggest that electron transfer from the reduced state of $HV^{\bullet+}$ to the excited $Eu(hfa)_3(TPPO)_2$ is not the primary cause of the luminescence quenching.

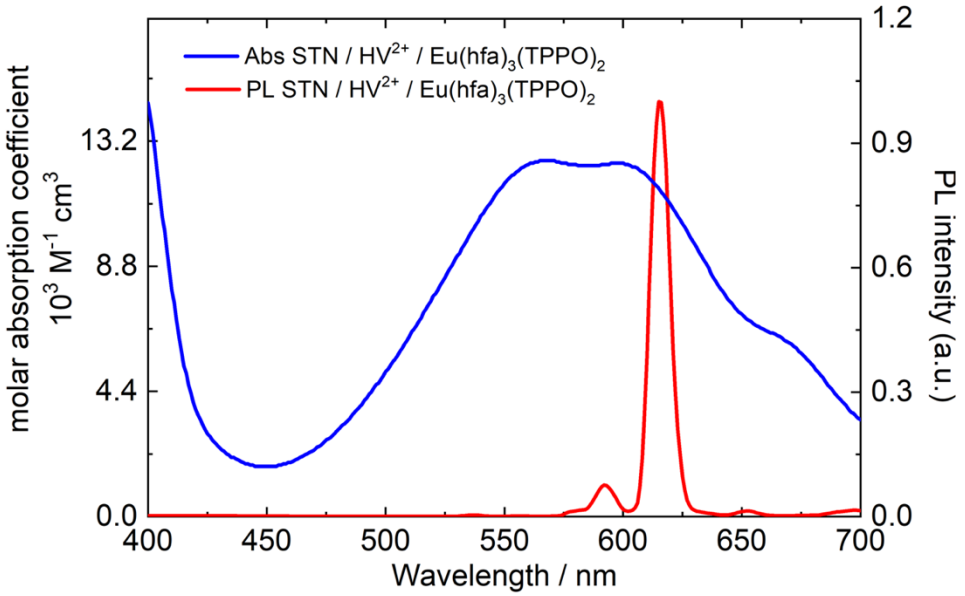

Figure 3-14 Absorption spectra under the application of -2.0 V (blue line) and normalized emission spectra of $Eu(hfa)_3(TPPO)_2$ (red line) under open circuit.

Photophysical parameters derived from the emission spectra (**Figure 3-11(b)**) were analyzed using LUMPAC software[138]. The I_{rel} value ($I_{rel} = I_{ED} / I_{MD}$) serves as an indicator of the site symmetry of Eu^{3+}, while the luminescence quantum efficiency of the Eu^{3+} excited state (Φ_{Ln}) is defined as $k_r/ (k_r + k_{nr})$[158]. As presented in **Table 3-1**, Irel remained unchanged at 13.05, confirming that the symmetrical structure of the Eu(III) complex remained intact upon voltage application. Consequently, the k_r value was unaffected by the applied voltage. However, a significant increase in the k_{nr} value and a decline in Φ_{Ln} suggest that excitation energy is readily transferred from the Eu(III) complex to the colored $HV^{\bullet+}$ species through a non-radiative process. The energy transfer efficiency can be determined using **Equation 2**.

$$E = 1 - \frac{\tau}{\tau_0} \qquad \text{(Equation 2)}$$

Here, E represents the energy transfer efficiency from the Eu(III) complex to the colored $HV^{\bullet+}$, while τ_0 and τ denote the luminescence lifetimes before and after voltage application, respectively. The luminescence lifetimes, obtained from **Figure 3-13(b)**, are summarized in **Table 3-1**, with the energy transfer efficiency calculated as 45.3% using **Equation 2**. However, despite this, the red luminescence of $Eu(hfa)_3(TPPO)_2$ was nearly completely quenched (99.3%) due to the EC reaction of HV^{2+} (**Figure 3-11(b)**). This discrepancy may arise from the direct absorption of emitted light by the colored $HV^{\bullet+}$ species, a phenomenon known as the inner filter effect, which contributes further to the reduction in emission intensity.

Table 3-1 Radiative transition rate (k_r), non-radiative transition rate (k_{nr}), symmetry factor (I_{rel}), intrinsic quantum efficiency (Φ_{Ln}), and emission lifetimes (τ_{ave}) of the STN/ HV^{2+}/ $Eu(hfa)_3(TPPO)_2$ device before and after voltage application.

	k_r (s^{-1})	k_{nr} (s^{-1})	Φ_{Ln} (%)	I_{rel}	τ_{ave}(ms)
open circuit	769	696	52.5	13.05	0.682
−2V/ 150 s	769	1911	28.7	13.05	0.373

For STN/HV^{2+}/$Eu(hfa)_3(TPPO)_2$-based device, the energy transfer pathways within the clay matrix were investigated by calculating the emission lifetime (τ), while the contribution (%) of each exponential component (τ_1, τ_2, and τ_3) was calculated from **Figure 3-13**. The results are summarized in **Table 3-2**. Prior to voltage application, the device exhibited a single-exponential emission lifetime of 682 μs. However, after applying voltage, the emission decay transitioned to a multi-exponential behavior,

comprising three components—τ_1, τ_2, and τ_3—contributing 24%, 36%, and 40%, respectively. The value of the longer lifetime τ_3 component (τ_3; 682 μs) was same as that of the single component before applying voltage, suggesting that it does not contribute to energy transfer to the colored $HV^{\bullet+}$ species. In contrast, the shorter lifetime components, $\tau_1$and τ_2, are associated with energy transfer to $HV^{\bullet+}$. Using **Equation 2**, the energy transfer efficiency for τ_1, τ_2 and τ_3 was calculated to be 92%, 65%, and 0, respectively. The total energy transfer from the τ_1, τ_2, and τ_3 components of the $Eu(hfa)_3(TPPO)_2$ complex to the colored $HV^{\bullet+}$ species was determined to be 45.5% (0.24 × 0.92 + 0.36 × 0.65 + 0.40 × 0), which is consistent with the value (45.3%) obtained from **Equation 2**, using the averaged luminescence lifetime (τ_{ave}).

Furthermore, the donor–acceptor distance (r_{DA}), the overlap integral J, and Förster distance (R_0) were calculated. As summarized in **Table 3-2**, the r_{DA} value for the τ_1 component is 4.75 nm, while for the τ_2, it is 6.44 nm. The average inter-anionic charge separation on the clay surface was approximately 1.2 nm[140]. However, actual intermolecular spacing within the clay layer varies depending on molecular size. Moreover, steric and electrostatic repulsions between adsorbed molecules can further increase these distances[159]. Within the interlayers of the STN matrix, 50% of the methyltri-n-octylammonium ions remained unexchanged, increasing the donor-acceptor distance. As a result, energy transfer between the colored $HV^{\bullet+}$ species and the $Eu(hfa)_3(TPPO)_2$ complex follows two distinct positional pathways. A schematic representation of the proposed energy transfer mechanism in the STN/HV^{2+}/$Eu(hfa)_3(TPPO)_2$-based device is shown in **Figure 3-15**. For the τ_1 component, energy transfer efficiency reached 92%, predominantly occurring within the same STN layer, where the $Eu(hfa)_3(TPPO)_2$ complex transfers energy to an adjacent $HV^{\bullet+}$ species. In contrast, the τ_2 component exhibited a r_{DA} of 6.44 nm, significantly exceeding the 1 nm thickness of an STN layer. Consequently, its energy transfer efficiency was lower (65%). This transfer likely occurs both within the same layer over a greater molecular distance and through vertical energy transfer between different STN layers.

Table 3-2 Emission lifetimes (τ), contribution (%) of the components, energy transfer efficiency (*E*), and donor-acceptor distance (r_{DA}) of STN/ HV^{2+}/ $Eu(hfa)_3(TPPO)_2$-based device before and after applying voltage

		τ_1(μs)	τ_2(μs)	τ_3(μs)
open circuit	emission lifetime	-	-	682
	contribution (%)	-	-	100
−2.0 V/150 s	emission lifetime	52	242	682
	contribution (%)	24%	36%	40%
	E (%)	92%	65%	0
	r_{DA}(nm)	4.75	6.44	-

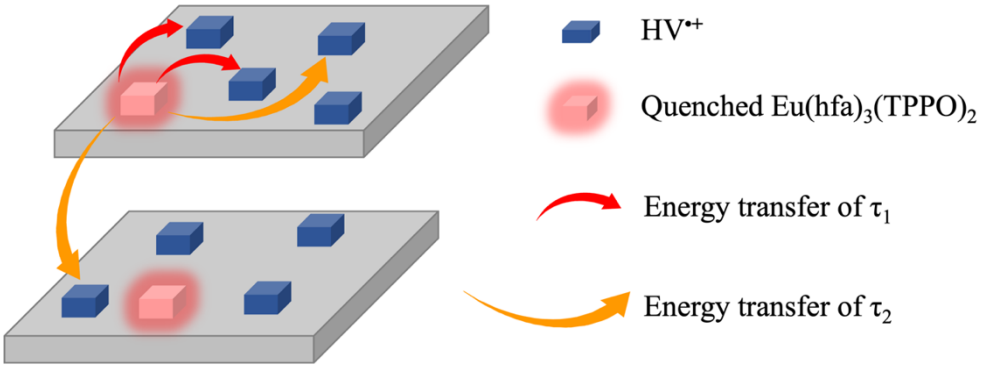

Figure 3-15 Schematic diagram of energy transfer between $HV^{\bullet+}$ and $Eu(hfa)_3(TPPO)_2$ between STN layers.

3.5 Summary

Chapter 3 explores the electrochemical properties of a luminescent $Eu(hfa)_3(TPPO)_2$ complex and an electrochromic HV^{2+} molecule integrated into a synthetic smectite (STN) matrix. Utilizing these hybrid materials, an electrically tunable luminescence and coloration device was developed. Initially, the intercalation and adsorption behaviors of the $Eu(hfa)_3(TPPO)_2$ complex and HV^{2+} molecule within the STN matrix were examined. The findings revealed that both components partially intercalated into the interlayer spaces of STN. When the molar ratio of STN to the $Eu(hfa)_3(TPPO)_2$ complex and HV^{2+} molecule was set at 50%:50% relative to the cation exchange capacity (CEC), approximately 80% of HV^{2+} and 20% of $Eu(hfa)_3(TPPO)_2$ were adsorbed onto the STN surface.

Next, the electrochemical properties of HV^{2+} and $Eu(hfa)_3(TPPO)_2$ within the STN matrix were investigated. The results showed that the $Eu(hfa)_3(TPPO)_2$ complex increased the interlayer spacing of STN, promoting electrolyte mobility and accelerating the reaction rate of HV^{2+}, thereby enhancing electrochromic performance. In the emission and coloration device, the red photoluminescence of $Eu(hfa)_3(TPPO)_2$ was clearly visible under open-circuit conditions. Upon applying a −2.0 V bias for 150 seconds, the electrochemically generated $HV^{\bullet+}$ species (cyan in color) efficiently quenched this red emission. Theoretical calculations suggested that the observed color modulation in the device was driven by energy transfer from the excited $Eu(hfa)_3(TPPO)_2$ complex to the colored $HV^{\bullet+}$ state, along with the reabsorption of emitted light by $HV^{\bullet+}$. This mechanism enabled the device to exhibit both emission and reflection properties.

Given these characteristics, we believe this dual-mode device offers promising potential for applications in advanced sensors and display technologies.

Chapter 4

Conclusion and Prospects

Chapter 4 Conclusion and Prospects

Since the late 18th century, luminescent lanthanide materials have garnered significant interest from numerous scientists. Over the past few centuries, substantial progress has been made in this field. The important advancements include the exploration of intramolecular energy transfer from organic ligands to lanthanide ions in the early 1960s, which established a foundation for the ongoing development of luminescent materials based on lanthanide complexes.

The flexible coordination environment surrounding Ln^{3+} ions, coupled with their high ionic characteristics, opens up numerous possibilities for lanthanide hybrid systems. The photoluminescent properties and stability of these materials can be significantly enhanced through hybridization with various matrix materials, resulting in improved luminescent performance and high stability. Additionally, with the advent of electroluminescent display devices, the construction of electroluminescent chromism devices has gained widespread acceptance due to their simple structure and ability to exhibit vivid photoluminescent changes across diverse materials and systems. Lanthanide materials are regarded as ideal candidates for electroluminescent chromism applications, and over the past decade, their performance in this area has been extensively investigated, encompassing the control of photoluminescent colors, on/off emission contrast, and switching stability.

In this doctoral dissertation, a comprehensive study was conducted on the photophysical properties and electroluminescent chromism characteristics of Eu(III) complex composites with smectite materials. Previous research has indicated that the photoluminescent performance of Eu(III) complexes is significantly enhanced upon hybridization with DNA, DNA-CTMA matrices, and alkyl ammonium salts. In this study, we employed a novel clay matrix material (smectite) and initially prepared $Eu(tta)_3phen$-smectite hybrid materials using a direct doping method. The photophysical properties of the hybrid materials in acetonitrile solution were systematically investigated. The results demonstrated that the interaction with smectite significantly improved the luminescent performance and quantum efficiency of $Eu(tta)_3phen$. This enhancement is attributed to the microenvironment provided by smectite, which interacts with $Eu(tta)_3phen$ and suppresses non-radiative transitions. Additionally, we incorporated the $Eu(tta)_3phen$/smectite hybrid material into a polymer (PMMA) matrix, resulting in a highly luminescent and transparent polymer film. With the addition of smectite, the film exhibited increased luminescent intensity while maintaining good transparency and uniform emission.

After investigating the photophysical properties, the electrofluorochromic reactions of the $Eu(hfa)_3(TPPO)_2$-smectite hybrid material were studied. The Eu(III) complex and HV^{2+} were dissolved in a STN-dispersed solution to study the interactions among the three components. The results demonstrated that a portion of the Eu(III) complex and HV^{2+} molecules were intercalated between the STN layers. By evaluating the adsorption capacities of different molecules on STN, it was found that approximately 80% of HV^{2+} and 20% of $Eu(hfa)_3(TPPO)_2$ were adsorbed onto STN in case50%:50% vs CEC. Subsequently, the luminescent Eu(III) complex and HV^{2+} were immobilized on an electrode in STN matrix, and the electrochemical properties of HV^{2+} and $Eu(hfa)_3(TPPO)_2$ within the STN matrix were studied. The results indicated that $Eu(hfa)_3(TPPO)_2$ expanded the interlayer spacing of STN, facilitating the movement of electrolytes and thereby enhancing the electrochromic performance of HV^{2+}. Under open-circuit conditions, the red photoluminescence of $Eu(hfa)_3(TPPO)_2$ was clearly observable. By applying a −2.0 V bias for 150 s, the electrochemically colored $HV^{\bullet+}$ species caused the device to exhibit a cyan color, while the red emission from $Eu(hfa)_3(TPPO)_2$ was quenched. The emission color change of the device was achieved through energy transfer from the excited state of $Eu(hfa)_3(TPPO)_2$ to the colored $HV^{\bullet+}$ state, as well as the reabsorption of luminescence by the colored $HV^{\bullet+}$ species, resulting in a device that exhibited dual emission and reflection modes through electrochemical reactions.

In summary, the hybridization of Eu(III) complexes with smectite enhances emission characteristics and promotes the development of electrofluorochromic devices. These advanced Eu(III) hybrid systems are characterized by their exceptional photoluminescent capabilities, demonstrating substantial promise for a variety of practical applications.

General Experimental

Reagents and Materials

All chemicals were commercially available and used as received. Smectite (Sumecton STN) was purchased from Kunimine Industries Co., Ltd. (Japan). The Eu(III) complex (1,10-phenanthroline)tris[4,4,4-trifluoro-1-(2-thienyl)-1,3-butanedionato]europium(III) ($Eu(tta)_3phen$) was purchased from Tokyo Chemical Industry Co., Ltd. (Japan). Polymethyl methacrylate (PMMA) was purchased from FUJIFILM Wako Pure Chemical Corporation (Japan). Acetonitrile was purchased from KANTO Chemical Co., Inc (Japan). Europium(III) acetate n-hydrate (99.9 %), hexafluoroacetylacetone (hfa-H2), triphenylphosphine oxide (TPPO), and the electrochromic molecule 1,1′-diheptyl-4,4′-bipyridinium dibromide (HV^{2+}) compound were purchased from Tokyo Chemical Industry Co., Ltd., Tokyo, Japan. Smectite (Sumecton STN) with a CEC of 60 meq/100 g was purchased from Kunimine Industries Co., Ltd., Tokyo, Japan. The Chemical formula of STN is $[(C_8H_{17})_3(CH_3)N]_{0.33}[(Mg_{2.67}Li_{0.33})Si_4O_{10}(OH)_2]$. Methyltri-n-octylammonium ions $[(C_8H_{17})_3(CH_3)N]_{0.33}$ are intercalated between the layers of smectite, resulting in its uniform dispersion in medium-to-high polar solvents. The plastic spacers were purchased from Lintec, Corporation, Tokyo, Japan. Propylene carbonate (PC), acetonitrile, and tetra-n-butylammonium perchlorate (TBAP) were purchased from KANTO Chemical Co., Inc., Tokyo, Japan. The $Eu(hfa)_3(TPPO)_2$ complex, synthesized according to a previously reported procedure[160], was used in this study.

Experimental instrumental

Oxygen dissolved in the solution was removed by bubbling nitrogen gas through the solution before carrying out the optical measurements. Absorption spectra and diffuse reflectance spectra were acquired using an ultraviolet–visible/near-infrared region (UV–visible/NIR) spectrophotometer with an integrated shell (V-770; JASCO Corporation, Japan). The luminescence spectra were recorded using a spectrofluorometer (FP-8500, JASCO Corporation, Japan). The emission lifetimes were determined using a time-resolved fluorescence spectrometer (Quantaurus-Tau C11367-21, Hamamatsu Photonics K. K., Japan). The surface profiles of the films were obtained using a multi-functional fully automatic micro-shape measuring machine (ET 4000A, Kosaka Laboratory Ltd., Japan). The supernatant was obtained by centrifugation at a speed of 11,000 rpm for 1 h using a centrifuge (AS185H, AS ONE Corporation, Japan). Powder X-ray diffraction (PXRD) was performed using an X-ray powder diffractometer (AXS D8 ADVANCE, Bruker AXS, Karlsruhe, Germany) with

a Cu Kα radiation source (λ = 1.5418Å), operating at 40 kV and 40mA. Cyclic voltammetry (CV) experiments and chronoamperometry experiments were performed at a scan rate of 50 mV/s^{-1} using a potentiostat/galvanostat (ALS660A; CH Instruments, Inc., Austin, TX, USA) controlled by a computer. The in-situ absorption spectra of the three- and two-electrode devices were recorded using a fiber-optic spectrometer system (USB2000, Ocean Optics, Orlando, FL, USA) during potential or voltage sweeping. Those measurements were conducted in the atmosphere of the laboratory.

Reference

[1] J.-C. G. Bünzli, *Coordination Chemistry Reviews* **2015**, *293-294*, 19.
[2] R. Reisfeld, C. K. Jorgensen, "*Lasers and excited states of rare earths"*, Springer Science & Business Media, 2012.
[3] C. K. Jørgensen, *Molecular Physics* **1962**, *5*, 271.
[4] G. H. Dieke, H. M. Crosswhite, *Appl. Opt.* **1963**, *2*, 675.
[5] K. Binnemans, *Coordination Chemistry Reviews* **2015**, *295*, 1.
[6] S. Faulkner, S. J. A. Pope, B. P. Burton-Pye, *Applied Spectroscopy Reviews* **2005**, *40*, 1.
[7] R. Carr, N. H. Evans, D. Parker, *Chemical Society Reviews* **2012**, *41*, 7673.
[8] L. Armelao, S. Quici, F. Barigelletti, G. Accorsi, G. Bottaro, M. Cavazzini, E. Tondello, *Coordination Chemistry Reviews* **2010**, *254*, 487.
[9] C. Benelli, P. Guerriero, S. Tamburini, P. A. Vigato, *Materials Chemistry and Physics* **1992**, *31*, 137.
[10] R. C. Leif, L. M. Vallarino, M. C. Becker, S. Yang, *Cytometry Part A* **2006**, *69A*, 767.
[11] M. A. Katkova, A. P. Pushkarev, T. V. Balashova, A. N. Konev, G. K. Fukin, S. Y. Ketkov, M. N. Bochkarev, *Journal of Materials Chemistry* **2011**, *21*, 16611.
[12] L. Li, J. Gou, D.-F. Wu, Y.-J. Wang, Y.-Y. Duan, H.-H. Chen, H.-L. Gao, J.-Z. Cui, *New Journal of Chemistry* **2020**, *44*, 3912.
[13] J. Yu, L. Zhou, H. Zhang, Y. Zheng, H. Li, R. Deng, Z. Peng, Z. Li, *Inorganic Chemistry* **2005**, *44*, 1611.
[14] S. I. Weissman, *The Journal of Chemical Physics* **1942**, *10*, 214.
[15] S. E. Bodman, S. J. Butler, *Chemical Science* **2021**, *12*, 2716.
[16] A. M. Kłonkowski, S. Lis, Z. Hnatejko, K. Czarnobaj, M. Pietraszkiewicz, M. Elbanowski, *Journal of Alloys and Compounds* **2000**, *300-301*, 55.
[17] N. Sabbatini, M. Guardigli, J.-M. Lehn, *Coordination Chemistry Reviews* **1993**, *123*, 201.
[18] S. I. Klink, G. A. Hebbink, L. Grave, P. G. B. Oude Alink, F. C. J. M. van Veggel, M. H. V. Werts, *The Journal of Physical Chemistry A* **2002**, *106*, 3681.
[19] B. Alpha, R. Ballardini, V. Balzani, J.-M. Lehn, S. Perathoner, N. Sabbatini, *Photochemistry and Photobiology* **1990**, *52*, 299.
[20] R. Devi, K. Singh, S. Vaidyanathan, *Journal of Materials Chemistry C* **2020**, *8*, 8643.
[21] H. Xu, Q. Sun, Z. An, Y. Wei, X. Liu, *Coordination Chemistry Reviews* **2015**, *293-294*, 228.
[22] L. Huang, K.-Z. Wang, C.-H. Huang, F.-Y. Li, Y.-Y. Huang, *Journal of Materials Chemistry* **2001**, *11*, 790.
[23] X.-N. Li, Z.-J. Wu, Z.-J. Si, Z. Liang, X.-J. Liu, H.-J. Zhang, *Physical Chemistry Chemical Physics* **2009**, *11*, 9687.
[24] C. Yang, J. Luo, J. Ma, D. Zhu, L. Miao, Y. Zhang, L. Liang, M. Lu, *Synthetic Metals* **2012**, *162*, 1097.
[25] T. B. Emelina, I. V. Kalinovskaya, A. G. Mirochnik, *Spectrochimica Acta Part A:*

Molecular and Biomolecular Spectroscopy **2019**, *207*, 222.
[26] L. Arrué, J. Santoyo-Flores, N. Pizarro, X. Zarate, D. Páez-Hernández, E. Schott, *Chemical Physics Letters* **2021**, *773*, 138600.
[27] N. Sabbatini, M. Guardigli, I. Manet, "Chapter 154 Antenna effect in encapsulation complexes of lanthanide ions", in *Handbook on the Physics and Chemistry of Rare Earths*, Elsevier, 1996, p. 69.
[28] R. D. Peacock, *Journal of Molecular Structure* **1978**, *46*, 203.
[29] G. Choppin, J. Bünzli, *CG Bunzli GR Choppin Elsevier Amsterdam* **1989**, *219*.
[30] W. C. Nieuwpoort, G. Blasse, *Solid State Communications* **1966**, *4*, 227.
[31] C. Görller-Walrand, K. Binnemans, "Chapter 167 Spectral intensities of f-f transitions", in *Handbook on the Physics and Chemistry of Rare Earths*, Elsevier, 1998, p. 101.
[32] C. K. Jørgensen, B. R. Judd, *Molecular Physics* **1964**, *8*, 281.
[33] C. Görller-Walrand, L. Fluyt, A. Ceulemans, W. T. Carnall, *The Journal of Chemical Physics* **1991**, *95*, 3099.
[34] E. E. S. Teotonio, H. F. Brito, M. C. F. C. Felinto, C. A. Kodaira, O. L. Malta, *Journal of Coordination Chemistry* **2003**, *56*, 913.
[35] K. Binnemans, C. Görller-Walrand, *J. Rare Earths* **1996**, *14*, 173.
[36] J. E. Lowther, *Journal of Physics C: Solid State Physics* **1974**, *7*, 4393.
[37] M. H. V. Werts, R. T. F. Jukes, J. W. Verhoeven, *Physical Chemistry Chemical Physics* **2002**, *4*, 1542.
[38] L. Liu, X. Chen, *Nanotechnology* **2007**, *18*, 255704.
[39] S. G. Prasanna Kumar, R. Hari Krishna, N. Kottam, P. Krishna Murthy, C. Manjunatha, R. Preetham, C. Shivakumara, T. Thomas, *Dyes and Pigments* **2018**, *150*, 306.
[40] B. R. Judd, *Physical Review* **1962**, *127*, 750.
[41] G. S. Ofelt, *The Journal of Chemical Physics* **1962**, *37*, 511.
[42] W. T. Carnall, H. Crosswhite, H. M. Crosswhite, "Energy level structure and transition probabilities in the spectra of the trivalent lanthanides in LaF_3", United States, 1978Medium: ED; Size: 195 p.
[43] R. D. Peacock, "The intensities of lanthanide f ↔ f transitions", in *Rare Earths*, E. Nieboer, C.K. Jørgensen, R.D. Peacock, and R. Reisfeld, Eds., Springer Berlin Heidelberg, Berlin, Heidelberg, 197583.
[44] S. V. Eliseeva, J.-C. G. Bünzli, *Chemical Society Reviews* **2010**, *39*, 189.
[45] J.-C. G. Bünzli, C. Piguet, *Chemical Society Reviews* **2005**, *34*, 1048.
[46] K. Binnemans, C. Görller-Walrand, *Chemical Reviews* **2002**, *102*, 2303.
[47] K. Binnemans, *Chemical Reviews* **2007**, *107*, 2592.
[48] K. Binnemans, *Chemical Reviews* **2009**, *109*, 4283.
[49] L. D. Carlos, R. A. S. Ferreira, V. d. Z. Bermudez, S. J. L. Ribeiro, *Advanced Materials* **2009**, *21*, 509.
[50] C. Sanchez, B. Lebeau, F. Chaput, J.-P. Boilot, *Advanced Materials* **2003**, *15*, 1969.
[51] K. Kuriki, Y. Koike, Y. Okamoto, *Chemical Reviews* **2002**, *102*, 2347.
[52] L.-N. Sun, H.-J. Zhang, Q.-G. Meng, F.-Y. Liu, L.-S. Fu, C.-Y. Peng, J.-B. Yu, G.-L. Zheng, S.-B. Wang, *The Journal of Physical Chemistry B* **2005**, *109*, 6174.

[53] L. Fu, R. A. S. Ferreira, S. S. Nobre, L. D. Carlos, J. Rocha, *Journal of Luminescence* **2007**, *122-123*, 265.
[54] T. Jin, S. Tsutsumi, Y. Deguchi, K. Machida, G. Adachi, *Journal of Alloys and Compounds* **1997**, *252*, 59.
[55] H. Li, D. Ueda, S. Inoue, K.-i. Machida, G.-y. Adachi, *Bulletin of the Chemical Society of Japan* **2002**, *75*, 161.
[56] M. Morita, S. Buddhudu, D. Rau, S. Murakami, "Photoluminescence and Excitation Energy Transfer of Rare Earth Ions in Nanoporous Xerogel and Sol-Gel SiO2 Glasses", in *Optical Spectra and Chemical Bonding in Transition Metal Complexes: Special Volume dedicated to Professor Jørgensen*, T. Schönherr, Ed., Springer Berlin Heidelberg, Berlin, Heidelberg, 2004, p. 115.
[57] G. Qian, M. Wang, *Journal of the American Ceramic Society* **2000**, *83*, 703.
[58] G. Qian, M. Wang, Z. Yang, *Journal of Physics and Chemistry of Solids* **2002**, *63*, 1829.
[59] G. Qian, Z. Yang, M. Wang, *Journal of Luminescence* **2002**, *96*, 211.
[60] X. Guo, H. Guo, L. Fu, L. D. Carlos, R. A. S. Ferreira, L. Sun, R. Deng, H. Zhang, *The Journal of Physical Chemistry C* **2009**, *113*, 12538.
[61] N. Lin, H. Li, Y. Wang, Y. Feng, D. Qin, Q. Gan, S. Chen, *European Journal of Inorganic Chemistry* **2008**, *2008*, 4781.
[62] H.-F. Lu, B. Yan, J.-L. Liu, *Inorganic Chemistry* **2009**, *48*, 3966.
[63] L. Sun, S. Dang, J. Yu, J. Feng, L. Shi, H. Zhang, *The Journal of Physical Chemistry B* **2010**, *114*, 16393.
[64] D. Wang, B. Li, L. Zhang, J. Ying, X. Wu, *Journal of Luminescence* **2010**, *130*, 598.
[65] Q. G. Meng, P. Boutinaud, A. C. Franville, H. J. Zhang, R. Mahiou, *Microporous and Mesoporous Materials* **2003**, *65*, 127.
[66] Q. Xu, L. Li, X. Liu, R. Xu, *Chemistry of Materials* **2002**, *14*, 549.
[67] S. Gago, J. A. Fernandes, J. P. Rainho, R. A. Sá Ferreira, M. Pillinger, A. A. Valente, T. M. Santos, L. D. Carlos, P. J. A. Ribeiro-Claro, I. S. Gonçalves, *Chemistry of Materials* **2005**, *17*, 5077.
[68] Y. Li, B. Yan, H. Yang, *The Journal of Physical Chemistry C* **2008**, *112*, 3959.
[69] L. Dolatyari, M. R. Yaftian, S. Rostamnia, *Journal of the Taiwan Institute of Chemical Engineers* **2016**, *60*, 174.
[70] Y.-J. Li, B. Yan, *Inorganic Chemistry* **2009**, *48*, 8276.
[71] X. Guo, X. Wang, H. Zhang, L. Fu, H. Guo, J. Yu, L. D. Carlos, K. Yang, *Microporous and Mesoporous Materials* **2008**, *116*, 28.
[72] A. M. Kaczmarek, Y. Maegawa, A. Abalymov, A. G. Skirtach, S. Inagaki, P. Van Der Voort, *ACS Applied Materials & Interfaces* **2020**, *12*, 13540.
[73] X. Guo, L. Fu, H. Zhang, L. D. Carlos, C. Peng, J. Guo, J. Yu, R. Deng, L. Sun, *New Journal of Chemistry* **2005**, *29*, 1351.
[74] S. Li, H. Song, W. Li, X. Ren, S. Lu, G. Pan, L. Fan, H. Yu, H. Zhang, R. Qin, Dai, T. Wang, *The Journal of Physical Chemistry B* **2006**, *110*, 23164.
[75] Y. Liu, L. Sun, J. Liu, Y.-X. Peng, X. Ge, L. Shi, W. Huang, *Dalton Transactions* **2015**, *44*, 237.

[76] B. Yan, *RSC Advances* **2012**, *2*, 9304.
[77] Y. Li, X. Yu, T. Yu, *Journal of Materials Chemistry C* **2017**, *5*, 5411.
[78] C. Peng, H. Zhang, J. Yu, Q. Meng, L. Fu, H. Li, L. Sun, X. Guo, *The Journal of Physical Chemistry B* **2005**, *109*, 15278.
[79] Z. Li, N. Hitomi, H. Tanaka, H. Ohmagari, K. Nakamura, M. Hasegawa, N. Kobayashi, *Materials Advances* **2024**, *5*, 1897.
[80] K. Nakamura, H. Minami, A. Sagara, N. Itamoto, N. Kobayashi, *Journal of Materials Chemistry C* **2018**, *6*, 4516.
[81] H. S. Santos, T. Laihinen, L. C. V. Rodrigues, J. Sinkkonen, E. Mäkilä, P. Damlin, L. K. O. Nakamura, H. F. Brito, J. Hölsä, M. Lastusaari, *Luminescence* **2019**, *34*, 23.
[82] M. M. Lezhnina, U. H. Kynast, *Optical Materials* **2010**, *33*, 4.
[83] A. Sánchez, Y. Echeverría, C. M. S. Torres, G. González, E. Benavente, *Materials Research Bulletin* **2006**, *41*, 1185.
[84] S. Celedon, C. Quiroz, G. Gonzalez, C. M. Sotomayor Torres, E. Benavente, *Materials Research Bulletin* **2009**, *44*, 1191.
[85] G. W. Brindley, R. Keith, *Mineralogical Magazine and Journal of the Mineralogical Society* **1946**, *27*, 242.
[86] R. J. King, *Geology Today* **2009**, *25*, 75.
[87] D. T. de Araujo, K. J. Ciuffi, E. J. Nassar, M. A. Vicente, R. Trujillano, P. S. Calefi, V. Rives, E. H. de Faria, *The Journal of Physical Chemistry C* **2017**, *121*, 5081.
[88] K. A. Jaradat, Z. Darbari, M. Elbakhshwan, S. L. Abdelaziz, S. K. Gill, E. Dooryhee, L. E. Ecker, *Applied Clay Science* **2017**, *150*, 163.
[89] F. Uddin, *Metallurgical and Materials Transactions A* **2008**, *39*, 2804.
[90] H. Cheng, Q. Liu, J. Yang, S. Ma, R. L. Frost, *Thermochimica Acta* **2012**, *545*, 1.
[91] O. Y. Golubeva, E. N. Korytkova, V. V. Gusarov, *Russian Journal of Applied Chemistry* **2005**, *78*, 26.
[92] D. Yang, J. Wang, H. Li, *Dyes and Pigments* **2015**, *118*, 53.
[93] Y. Yao, Z. Li, H. Li, *RSC Advances* **2015**, *5*, 70868.
[94] Y. Wang, P. Li, S. Wang, H. Li, *Journal of Rare Earths* **2019**, *37*, 451.
[95] J. Ma, D. Yang, X. Song, Y. Wang, *Journal of Luminescence* **2019**, *212*, 126.
[96] Y. Ma, H. Wang, W. Liu, Q. Wang, J. Xu, Y. Tang, *The Journal of Physical Chemistry B* **2009**, *113*, 14139.
[97] J. Xu, Y. Zhang, H. Chen, W. Liu, Y. Tang, *Dalton Transactions* **2014**, *43*, 7903.
[98] J. Xu, Z. Sun, L. Jia, B. Li, L. Zhao, X. Liu, Y. Ma, H. Tian, Q. Wang, W. Liu, Y. Tang, *Dalton Transactions* **2011**, *40*, 12909.
[99] J. Xu, X. Shen, L. Jia, C. Zhang, T. Ma, T. Zhou, T. Zhu, Z. Xu, J. Cao, B. Liu, N. Bi, L. Liu, Y. Li, *Dyes and Pigments* **2018**, *148*, 44.
[100] J. Xu, X. Shen, L. Jia, T. Zhou, T. Ma, Z. Xu, J. Cao, Z. Ge, N. Bi, T. Zhu, S. Guo, X. Li, *Journal of Hazardous Materials* **2018**, *342*, 158.
[101] P. A. Alaba, Y. M. Sani, W. M. Ashri Wan Daud, *RSC Advances* **2015**, *5*, 101127.
[102] E. H. de Faria, O. J. Lima, K. J. Ciuffi, E. J. Nassar, M. A. Vicente, R. Trujillano, P. S. Calefi, *Journal of Colloid and Interface Science* **2009**, *335*, 210.
[103] E. H. de Faria, E. J. Nassar, K. J. Ciuffi, M. A. Vicente, R. Trujillano, V. Rives, P. S. Calefi, *ACS Applied Materials & Interfaces* **2011**, *3*, 1311.

[104] S.-J. Ryu, A. Kim, M. D. Kim, S. W. Hong, S. S. Min, J.-H. Lee, J.-K. Lee, H. Jung, *Applied Clay Science* **2014**, *101*, 52.
[105] D. Yang, Y. Wang, Y. Wang, Z. Li, H. Li, *ACS Applied Materials & Interfaces* **2015**, *7*, 2097.
[106] X. Chen, Y. Wang, R. Chai, Y. Xu, H. Li, B. Liu, *ACS Applied Materials & Interfaces* **2017**, *9*, 13554.
[107] D. Yang, Y. Wang, Y. Wang, H. Li, *Sensors and Actuators B: Chemical* **2016**, *235*, 206.
[108] P.-Y. Chiang, P.-H. Zeng, Y.-C. Yeh, *International Journal of Biological Macromolecules* **2024**, *260*, 129359.
[109] L. Hu, Q. Zhang, X. Li, M. J. Serpe, *Materials Horizons* **2019**, *6*, 1774.
[110] Y. S. Lui, W. T. Sow, L. P. Tan, Y. Wu, Y. Lai, H. Li, *Acta Biomaterialia* **2019**, *92*, 19.
[111] K. Ogasawara, K. Nakamura, N. Kobayashi, *Journal of Materials Chemistry C* **2016**, *4*, 4805.
[112] S. Hirata, K.-S. Lee, T. Watanabe, *Advanced Functional Materials* **2008**, *18*, 2869.
[113] V. Goulle, A. Harriman, J.-M. Lehn, *Journal of the Chemical Society, Chemical Communications* **1993**, 1034.
[114] D. Aigner, S. M. Borisov, I. Klimant, *Analytical and Bioanalytical Chemistry* **2011**, *400*, 2475.
[115] R. M. Clegg, "Chapter 1 Förster resonance energy transfer—FRET what is it, why do it, and how it's done", in *Laboratory Techniques in Biochemistry and Molecular Biology*, Elsevier, 2009, p. 1.
[116] V. Rai, R. S. Singh, D. J. Blackwood, D. Zhili, *Advanced Engineering Materials* **2020**, *22*, 2000082.
[117] O. V. Mikhnenko, P. W. M. Blom, T.-Q. Nguyen, *Energy & Environmental Science* **2015**, *8*, 1867.
[118] A. Monguzzi, R. Tubino, F. Meinardi, *Physical Review B* **2008**, *77*, 155122.
[119] M. Chang, W. Chen, H. Xue, D. Liang, X. Lu, G. Zhou, *Journal of Materials Chemistry C* **2020**, *8*, 16129.
[120] Y. Kim, H. Ohmagari, A. Saso, N. Tamaoki, M. Hasegawa, *ACS Applied Materials & Interfaces* **2020**, *12*, 46390.
[121] K. Su, N. Sun, Z. Yan, S. Jin, X. Li, D. Wang, H. Zhou, J. Yao, C. Chen, *ACS Applied Materials & Interfaces* **2020**, *12*, 22099.
[122] W. Gao, T. Yu, Y. Du, R. Wang, L. Wu, L. Bi, *ACS Applied Materials & Interfaces* **2016**, *8*, 11621.
[123] B. Wang, L.-H. Bi, L.-X. Wu, *Journal of Materials Chemistry* **2011**, *21*, 69.
[124] Y. Kim, J. Do, E. Kim, G. Clavier, L. Galmiche, P. Audebert, *Journal of Electroanalytical Chemistry* **2009**, *632*, 201.
[125] Y. Kim, E. Kim, G. Clavier, P. Audebert, *Chemical Communications* **2006**, 3612.
[126] F. Miomandre, P. Audebert, *Journal of Photochemistry and Photobiology C: Photochemistry Reviews* **2020**, *44*, 100372.
[127] K. Nakamura, K. Kanazawa, N. Kobayashi, *Chemical Communications* **2011**, *47*, 10064.

[128] K. Nakamura, K. Kanazawa, N. Kobayashi, *Displays* **2013**, *34*, 389.
[129] K. Kanazawa, K. Nakamura, N. Kobayashi, *Journal of Materials Chemistry C* **2015**, *3*, 7135.
[130] B. Rajamouli, P. Sood, S. Giri, V. Krishnan, V. Sivakumar, *European Journal of Inorganic Chemistry* **2016**, *2016*, 3900.
[131] G. Zhang, L. Mei, J. Ding, K. Su, Q. Guo, G. Lv, L. Liao, *Journal of Rare Earths* **2022**, *40*, 1360.
[132] L. U. Khan, D. Muraca, H. F. Brito, O. Moscoso-Londoño, M. C. F. C. Felinto, K. R. Pirota, E. E. S. Teotonio, O. L. Malta, *Journal of Alloys and Compounds* **2016**, *686*, 453.
[133] A. R. Sharits, J. F. Khoury, P. M. Woodward, *Inorganic Chemistry* **2016**, *55*, 12383.
[134] P. A. Tanner, *Chemical Society Reviews* **2013**, *42*, 5090.
[135] N. M. Shavaleev, S. V. Eliseeva, R. Scopelliti, J.-C. G. Bünzli, *Inorganic Chemistry* **2015**, *54*, 9166.
[136] H. R. Li, J. Lin, H. J. Zhang, L. S. Fu, Q. G. Meng, S. B. Wang, *Chemistry of Materials* **2002**, *14*, 3651.
[137] H.-G. Liu, S. Park, K. Jang, W.-S. Zhang, H.-J. Seo, Y.-I. Lee, *Materials Chemistry and Physics* **2003**, *82*, 84.
[138] J. D. L. Dutra, T. D. Bispo, R. O. Freire, *Journal of Computational Chemistry* **2014**, *35*, 772.
[139] F. Cagnin, M. R. Davolos, E. E. Castellano, *Polyhedron* **2014**, *67*, 65.
[140] Y. Ishida, *Bulletin of the Chemical Society of Japan* **2021**, *94*, 2886.
[141] Y. Ishida, T. Shimada, H. Tachibana, H. Inoue, S. Takagi, *The Journal of Physical Chemistry A* **2012**, *116*, 12065.
[142] A. Beneduci, S. Cospito, M. L. Deda, G. Chidichimo, *Advanced Functional Materials* **2015**, *25*, 1240.
[143] C.-P. Kuo, M.-k. Leung, *Physical Chemistry Chemical Physics* **2014**, *16*, 79.
[144] W. Gao, Q. Zhou, Z. Fu, T. Yu, L. Bi, *Electrochimica Acta* **2019**, *317*, 139.
[145] T. Fujimura, T. Shimada, S. Hamatani, S. Onodera, R. Sasai, H. Inoue, S. Takagi, *Langmuir* **2013**, *29*, 5060.
[146] Z. Klapyta, T. Fujita, N. Iyi, *Applied Clay Science* **2001**, *19*, 5.
[147] M. Alexandre, P. Dubois, *Materials Science and Engineering: R: Reports* **2000**, *28*, 1.
[148] Y. Hasegawa, Y. Wada, S. Yanagida, H. Kawai, N. Yasuda, T. Nagamura, *Applied Physics Letters* **2003**, *83*, 3599.
[149] Z. Li, K. Nakamura, N. Kobayashi, *Journal of Materials Chemistry C* **2023**, *11*, 118.
[150] Y.-Y. Wang, L. Song, S.-Y. Tang, Z.-Q. Dai, J.-Y. Guo, H.-Y. Shen, W.-X. Chai, *Materials Today Communications* **2022**, *32*, 104054.
[151] Y.-Y. Wang, L. Song, J.-T. Wang, Y.-M. Zhou, Z.-Q. Dai, W. Liu, J.-Y. Guo, H.-Y. Shen, W.-X. Chai, *Applied Organometallic Chemistry* **2022**, *36*, e6752.
[152] R. Ilmi, D. Zhang, L. Tensi, H. Al-Sharji, N. K. Al Rasbi, A. Macchioni, L. Zhou, W.-Y. Wong, P. R. Raithby, M. S. Khan, *Dyes and Pigments* **2022**, *203*, 110300.

[153] R. J. Mortimer, J. R. Reynolds, *Displays* **2008**, *29*, 424.
[154] M. Eguchi, M. Momotake, F. Inoue, T. Oshima, K. Maeda, M. Higuchi, *ACS Applied Materials & Interfaces* **2017**, *9*, 35498.
[155] K. Kanazawa, Y. Komiya, K. Nakamura, N. Kobayashi, *Physical Chemistry Chemical Physics* **2017**, *19*, 16979.
[156] K. Nakamura, N. Yanagawa, N. Kobayashi, *Journal of the Society for Information Display* **2022**, *30*, 15.
[157] K. Kanazawa, K. Nakamura, N. Kobayashi, *ChemistrySelect* **2018**, *3*, 9672.
[158] H. Minami, M. Miyazato, Z. Li, K. Nakamura, N. Kobayashi, *Chemical Communications* **2020**, *56*, 13532.
[159] S. Takagi, T. Shimada, Y. Ishida, T. Fujimura, D. Masui, H. Tachibana, M. Eguchi, H. Inoue, *Langmuir* **2013**, *29*, 2108.
[160] K. Nakamura, N. Yanagawa, N. Kobayashi, *Materials* **2022**, *15*, 5202.